DISLOCATION STRUCTURES AND DUCTILE FRACTURE OF COMMERCIAL COPPER TENSILE SPECIMENS

by

Ambra J. Shume

A Thesis

Submitted to the Faculty of Graduate Studies

in Partial Fulfillment of the Requirements

for the Degree of

MASTER OF SCIENCE

Department of Mechanical Engineering

University of Manitoba

Winnipeg, Manitoba, Canada

ISBN 0-315-54904-1

DISLOCATION STRUCTURES AND DUCTILE FRACTURE OF COMMERCIAL COPPER TENSILE SPECIMENS

BY

AMBRA J. SHUME

A thesis submitted to the Faculty of Graduate Studies of the University of Manitoba in partial fulfillment of the requirements of the degree of

MASTER OF SCIENCE

ABSTRACT

The development of low energy dislocation structures, in FCC metals subjected to tensile loading, has been established up to and during stage II of work hardening. The present study addresses the development of dislocation cells at high strains, during stage III of work hardening. The meshlength theory, which relates the formation of low energy dislocation structures to work hardening, is applied as a basis for understanding the development of dislocation cells.

Commercial purity copper tensile specimens exhibited work hardening during severe plastic deformation preceding fracture. They were examined to identify dislocation cell development and mechanisms responsible for final fracture. The fractured halves of cylindrical specimens were sectioned to produce a series of TEM foils of consecutive reduction in area values. Dislocation cell measurements revealed similitude, as predicted by the meshlength theory of work hardening. Initial cell size was influenced by grain size. Dislocation cell size decreased by hierarchical subdivision, until a characteristic minimum cell size of 0.4 μm was attained at 40% reduction in area. Subgrain formation was also observed, at the highest reduction in area values.

SEM examination of the fracture surfaces indicated that final fracture was triggered by void initiation at particle sites. Void initiation occurred by particle-matrix decohesion or brittle particle fracture, depending on particle size. Fracture surface dimples resulted from void growth and coalescence. Dislocation cells played a fundamental role during severe plastic deformation, but were not involved in the final fracture process.

ACKNOWLEDGEMENTS

This study was performed with the cooperation of dedicated personnel at the Mechanical Engineering Department, University of Manitoba. The author would like to especially thank Dr. M.N. Bassim for supervision of this thesis and for his continuous support and helpful contributions. Technical support provided by Yu Jun Zhang, Roy Hartle, John van Dorp, Don Mardis, and Ron Crampton are also gratefully acknowledged.

Financial support from the Department of Mechanical Engineering, University of Manitoba, and a fellowship from the Transport Institute are recognized and appreciated.

TABLE OF CONTENTS

LIST OF FIGURES

LIST OF SYMBOLS

σ	true stress
σ_y	yield stress
σ_o	frictional stress
s	engineering stress
τ	flow stress
τ_o	frictional shear stress
ε	true strain
e	engineering strain
G	shear modulus
υ	Poisson's ratio
b	Burgers vector
ρ	dislocation density
L	dislocation cell size
l	distance between individual dislocations
l'	average dislocation link length
l_s	link length of a multiplying dislocation
R	outer radius
r_o	dislocation core
D	grain size
E_{el}	dislocation line energy
W_F	work of fracture
γ_s	surface free energy
γ_B	energy of dislocation cell interface
N	number of dislocations in a pile-up

n	strain hardening coefficient
K	strength coefficient
k	constant
α	constant
g	proportionality constant
m	general exponent
μm	micrometer

BCC	Body-Centered Cubic
EDX	Energy Dispersive X-Ray
FCC	Face-Centered Cubic
LEDS	Low Energy Dislocation Structures

1. INTRODUCTION

The usefulness of an engineering material is determined by its ability to sustain an applied load. An ideal elastic-plastic metal is unable to carry a load greater than its yield strength. Work hardening metals are able to carry loads which exceed yield strength by undergoing microstructural changes which strengthen the metal. Extensive dislocation structures form when yield strength is exceeded. The present study examines microstructural aspects of work hardening in commercial copper due to tensile straining and the fracture process of this metal.

A work hardening metal becomes increasingly resistant to deformation when it deforms plastically. Work hardening is attributed to the presence, movement, and multiplication of dislocations. The complexity with which dislocations interact causes vivid patterns of dislocations to develop. Many dislocation structure studies focus on the conditions responsible for initial dislocation cell development [1]. Of equal interest, and the subject of this thesis, is the behaviour of developed dislocation structures at high strains. Examination of dislocation structures at high strains reveals characteristics of their evolution and points towards the mechanical contribution of these structures during deformation and fracture.

Dislocation structures in metals serve two needs during straining, namely energy minimization and the accommodation of increasing dislocation density [2]. The dislocation structures resulting from uniaxial tension in copper are near circular cells. The cells become better defined and shrink in size as the copper is further strained. In this thesis, the meshlength theory of work hardening is applied to the development of dislocation cells in FCC metal deformed by a monotonically increasing tensile load.

Under certain circumstances, dislocation structures play a significant role in the fracture process, as well as plastic deformation. Typical failure modes resulting from monotonically increasing tensile load include localized shear, ductile fracture by void growth, cleavage and brittle intergranular fracture [3]. In cases where typical failure modes are suppressed or are not applicable, the path of a propagating crack follows the dislocation rich walls of dislocation structures [4]. Fracture triggered by dislocation structures implies that no other fracture mechanism is more critical. However, fracture is often initiated by mechanisms unrelated to the dislocation structure, and when this occurs dislocation structure development is halted abruptly. This is one of the difficulties of studying dislocation structures at high strains.

The present study illustrates dislocation behaviour in commercial purity copper subjected to tensile loading and determines the fracture process of the material. Tensile specimens are pulled to failure at constant crosshead speeds. The role of dislocation cells during plastic deformation and the fracture process is determined using transmission electron microscopy and scanning electron microscopy. Supplementary information, such as microhardness measurements and inclusion content, reinforces the analyses of deformation and fracture. The results are discussed in light of current theories of work hardening.

2. LITERATURE SURVEY

Plastic deformation and ductile fracture are broad areas of study. Aspects of both of these subjects are discussed in this thesis. Dislocation behaviour during plastic deformation is described by several work hardening theories. The meshlength theory of Kuhlmann-Wilsdorf is considered in most detail in the present study. Ductile fracture is addressed, as the test specimens in this study failed in this mode. The influences of dislocation structures and inclusions are considered during internal void initiation and growth.

2.1 Work Hardening Theory

The ability of a metal to deform is due to the existence of mobile dislocations. Dislocation distribution in a material is nonuniform, creating microscopic areas of high stress. From basic dislocation theory, it is shown that an applied shear stress of sufficient magnitude induces the movement of dislocations [5]. Thus, strain occurs at a stress much less than the theoretical shear stress. Resistance to dislocation movement increases the stress necessary for strain.

The free energy of a metal is minimized as it deforms plastically. Most energy dissipates as heat, but some energy is used to move dislocations and create low energy dislocation structures (LEDS). The interaction of dislocations causes some dislocations to become immobile. More stress is required to induce further strain, due to the increase of immobile dislocations. This feature of increased stress level required to further deform a metal is called work hardening. Several theories have been devised to explain this phenomenon.

The earliest work hardening theory is that of Taylor [6]. Taylor attributed the increasing resistance of further deformation to dislocation interaction. This theory assumes a uniform distribution of edge dislocations. The stress required for two edge dislocations to pass each other is inversely proportional to the distance between them. Mathematically, this is written as:

$$\tau = kGb(l^{-1}) \tag{1}$$

where τ is the flow stress, k is a constant, G is the shear modulus, b is the Burgers vector, and l is the distance between two dislocations. The applied shear stress is insufficient to induce movement when the dislocations are close enough to mutually trap each other. Both dislocations are immobilized. Accumulation of immobile dislocations causes an increase in internal stress, which increases the flow stress. Assuming a uniform dislocation spacing, Equation (1) is rewritten to show the relationship between flow stress and dislocation density, ρ.

$$\tau = kGb(\rho^{1/2}) \tag{2}$$

Taylor's work assumes shear stress is proportional to the square root of shear strain. This is consistent with the parabolic stress-strain curve generally accepted at that time. The theory of Taylor is inconsistent with the inhomogeneous dislocation distributions observed in experimentation. However, the idea of dislocation interaction being responsible for work hardening is the basis of subsequent work hardening theories.

Mott [7] modified Taylor's theory to account for the nonhomogeneous dislocation distribution. Mott replaced the individual dislocations of Taylor with dislocation pile-ups created from Frank-Read sources. A dislocation pile-up can be treated as a single dislocation with N times the size and N times the stress acting on the lead dislocation. The variable N is the number of dislocations present in the pile-up [8]. Mott defined the

obstacle responsible for trapping dislocations to be Lomer-Cottrell barriers. Thus, the formation of alternating areas of dislocation free areas and dense dislocation areas was accounted for. Mott's theory does have deficiencies. Notably, the number of dislocations required in a pile-up to make this theory work is too large to be reasonable [9]; about 1000 dislocations per pile-up are necessary.

The preliminary theories of Taylor and Mott are based on a parabolic stress-strain curve. Later research revealed a three stage work hardening curve for single crystals. The three stages, as depicted in Figure 2.1, are easy glide, linear hardening, and parabolic hardening [10,11]. The work hardening curve for polycrystals includes stages II and III, but stage I does not occur. The three stages of work hardening are generally accepted today, and a recently identified stage IV is being investigated [12].

Early studies of the three stage work hardening curve emphasize stages I and II. Detailed analysis of the movement of individual dislocations and factors influencing mobility are given considerable attention [13,14]. Analysis of the mobility of individual dislocations provides much understanding of the factors affecting the work hardening rate and the formation of dislocation structures, but becomes a difficult analysis technique to define the subsequent evolution of the dislocation structures. As a result, stage III of work hardening is often not addressed. Prominent work hardening theories based on the examination of individual dislocations are mentioned in the remainder of this section. The study of work hardening in terms of dislocation structures is discussed in Section 2.2.

A host of factors associated with dislocation movement during work hardening is characterized by Seeger [9,15,16] . Stage I has long, straight edge dislocations which lie on well defined primary slip planes. The lack of curved dislocations indicates the absence of long range internal stresses. The number of dislocation sources is considered

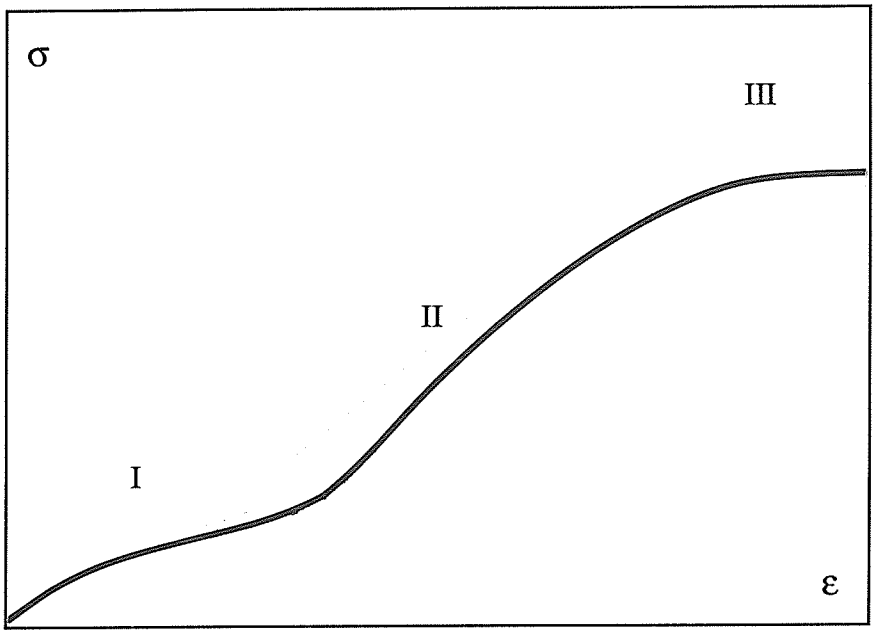

Figure 2.1: Generalized Three Stage Work Hardening Curve

(Figure from Reference [11].)

to be fixed, and stress increments cause dislocation generation. Dislocation generation ceases and stage I ends when the increment in back stress, caused by the new dislocations, equals the increment in applied stress.

Activation of secondary slip systems and an increase in hardening indicates the beginning of stage II. Lomer-Cottrell locks, which pin dislocations, are able to form with two active glide planes. Primary dislocations become curved, indicating long range stresses. The barriers on the primary slip system cause dislocation pile-ups. These pile-ups are considered to be superdislocations, and Seeger uses superdislocations to define flow stress in stage II. Superdislocations of greater size or smaller spacing require more stress to move, and, therefore, allow the high stresses of stage II to be achieved. Not all materials exhibit dislocation pile-ups, and Seeger acknowledges that similar results may be achieved with other dislocation structures, such as dislocation grids and braids [16].

Basinski and Basinski do not agree that secondary glide begins in stage II [17]. They state that glide in stage I is not restricted to the primary slip plane. A forest system exists, in addition to the primary slip system, encompassing the other active dislocations. Basinski and Basinski used etch pit experiments and electron microscope observations to identify forest dislocations in stage I.

Forest dislocations do not contribute significantly to the total strain in stage I, since the mean free path in the direction perpendicular to the primary glide plane is severely limited by the forest dislocation arrangements. The shortened mean slip distance causes a significant increase in flow stress. Three dimensional networks of forest dislocations become the major dislocation feature during stage II. Basinski and Basinski apply the relation of proportionality between flow stress and the square root of dislocation density to forest dislocations. Their work shows a relationship between flow stress and forest dislocation density, even in stage I.

Hirsch and Mitchell [18] report on carpets of dislocations in FCC and BCC materials during early stage II. According to their theory, primary dislocation pile-ups interact with secondary dislocations to form dislocation carpets in the primary plane. The carpets are made up of both primary and secondary dislocations and are occasionally joined by short segments or walls of dislocations which are perpendicular to the carpets. Using stress field calculations of dislocation arrangements, Hirsch and Mitchell relate the work hardening rate during stage II to the dislocation configuration and density in the carpets.

Clustering of dislocations into high and low density areas during stage II forms a variety of distinctive, reproducible patterns. The type of dislocation arrangements formed depends on the material and the loading condition. For example, a veining structure, containing alternating regions of dense dislocations and dislocation free material, is commonly found in fatigued metal [19]. A distinctive labyrinth structure composed of angled rectangular dislocation cells is produced from cyclic deformation of FCC steel [20]. Polycrystalline copper forms dislocation cells when fatigued [21]. Metals subjected to extreme wear exhibit dislocation cell and subgrain formation [22]. In metals which have undergone unidirectional straining, dislocation cells are prevalent [23]. The technique of studying individual dislocations becomes cumbersome and impractical with the formation of dislocation structures. An alternate approach to the study of work hardening becomes advantageous.

2.2 Meshlength Theory of Work Hardening

As work hardening progresses into stage II, dislocation structures form. Unlike the study of individual dislocations, the study of dislocation structures is well suited to address the high dislocation densities encountered in stages II and III. The meshlength

theory of work hardening [2,24] identifies the prevalent dislocation structure, not the individual dislocations, as the fundamental unit to describe the progression of work hardening in a metal. The sequence of dislocation structure development, in accordance with the meshlength theory, is described in the following sections.

2.2.1 Energy Minimization

Dislocation structures develop and evolve during work hardening. The meshlength theory describes the formation of low energy dislocation structures (LEDS) by a process of energy minimization. The study of LEDS provides valuable information for two areas of fundamental investigation: identification of classic dislocation structures; and understanding the relationship between energy minimization and the formation of LEDS.

The meshlength theory is based on energy minimization. Dislocations multiply and move about the metal to produce a quasiuniform distribution during stage I of work hardening. LEDS evolve during stage II, following a sequence of energy minimization. The one assured feature of an LEDS is that it is an energetically favourable dislocation arrangement enabling mutual stress screening of individual dislocations. Geometrical distributions of dislocations within LEDS may vary, depending on the stress condition. The evolution of LEDS is characterized by a continuous decrease in dislocation line energy.

A comparison of line energies for a series of dislocation structures was performed by Hansen and Kuhlmann-Wilsdorf [23]. It was shown that the natural development of dislocation arrangements is a sequence of line energy minimization. The basic equation

for line energy of a dislocation per unit length is:

$$E_{el} = \{Gb^2/4\}\, f(\upsilon)\, \ln(R/r_o) \qquad (3)$$

where G is the shear modulus, b is the magnitude of the Burgers vector, r_o is the core radius, R is the outer radius, υ is Poisson's ratio, and $f(\upsilon)$ is unity for a pure screw dislocation and $(1/(1-\upsilon))$ for a pure edge dislocation [5].

The dislocation structures listed in order of decreasing line energy are: random dislocation tangle, pile-up, dipolar mat, Taylor lattice, tilt wall, dipolar wall, and dislocation boundary of more than one Burgers vector [23]. This sequence is based on decreasing line energies, but may also reflect specific energies if long range stresses are negligible. The assumption of minimal long range stresses is maintained and defended by Kuhlmann-Wilsdorf [23,25,26]. The sequence of dislocation arrangements listed above indicates a series of states which dislocations may evolve into, in order to step-wise reduce their line energy.

2.2.2 LEDS Evolution in Stages I and II

A random distribution of dislocations rearranges into clusters of dislocations when a unidirectional stress is applied during easy glide in stage I. In a single glide system, the dislocations glide in one of two directions, depending on the sign of their Burgers vector. Local surpluses of similar dislocations form dipolar mats. The dipolar mat configuration is similar to an imperfect Taylor's lattice and provides energy reduction by mutual stress screening between dislocations. The dislocations multiply as the material is strained further, and the dislocation density within the dipolar mats increases. Accordingly, the long range tensile or compressive stress between the dipolar mats also increases.

The long range stresses present in the dipolar arrays may be relieved by activation of secondary glide dislocations, as described by Kuhlmann-Wilsdorf and Comins [26]. The dipolar mat arrangement of primary dislocations accommodates new primary dislocations in the same plane. The dislocation spacing within the primary planes eventually becomes smaller than the spacing between them. The number of active primary planes does not increase fast enough to relieve the local in-plane accumulation of dislocations. The compressive and tensile stresses which alternate between the primary glide planes, due to the dipolar arrangement of dislocations, are eventually eased by the onset of secondary glide.

The arrangement of dislocations during stage I for the case of an FCC metal with low stacking fault energy has been verified experimentally [26]. For this case, primary glide dislocations were found to initially form pile-ups and then distribute throughout the material in arrays representing imperfect Taylor lattices [27]. The long range tensile or compressive stresses present between the dipolar mats necessitate the activation of a second glide system for relief. Kuhlmann-Wilsdorf and Comins [26] found that one of the two secondary glide systems is usually predominant, leaving a tilt or twist component within the mat. Long range stresses remaining in the material are minimal. Kuhlmann-Wilsdorf and Comins have shown that long range stresses present after the onset of secondary glide are at least seven times less than the short range stress, and under ideal conditions would be zero.

Stage II of work hardening commences with the arrival of secondary dislocations [23,26]. Secondary glide continues until long range stresses within the secondary system are reduced to frictional stress. The interaction of primary and secondary dislocations leads to the formation of small angle boundaries. Small angle boundary structure is required on the primary system to obtain the conditions associated with negligible long

range stress. Ideally, tilt walls free of long range stresses would result, however some long range stresses remain in real crystals. The small angle boundaries mark the origin of dislocation cells.

The involvement of secondary dislocations reduces short range stresses, in addition to relieving long range stresses between dipolar mats. Primary and secondary dislocations interact to form Lomer-Cottrell locks. Kuhlmann-Wilsdorf and Comins [26] have shown that for FCC metals with low stacking fault energy, the participating secondary dislocation link length is shortened during the formation of a Lomer-Cottrell lock. The shorter dislocation link length ideally reduces dislocation line energy by the fraction 2.5/3. This process occurs spontaneously, since it is energetically favourable.

Dipolar mats transform into tilt walls and dipolar walls and eventually into dislocation cell walls, with the involvement of secondary dislocations [23]. The formation of dislocation cell walls is reviewed, as follows. Carpets of high dislocation density exist in the form of dipolar mats, prior to the onset of secondary glide. With secondary glide, the dislocations react to build fences joining the carpets. The fences consist basically of dipolar walls, which are tilt walls with ability for stress screening. The primary dislocations within the carpets rotate away from edge orientation and form Lomer-Cottrell locks with the secondary dislocations. The formation of carpets and fences enclose areas which are essentially dislocation free. Fully developed, this structure is recognized as a dislocation cell structure.

Dislocation cells, derived from the formation of carpets and walls of dislocations, are low energy dislocation structures [8]. Regions of dislocation free material rotated relative to one another and separated by dislocation walls have been mathematically modelled by Bassim [28], who has shown that such structures minimize long range and short range stresses [29]. A three-dimensional arrangement of cubic dislocation cells was

found to be the configuration of lowest energy [30]. In three-dimensional checkerboard pattern, the dislocations cells are rotated about a common axis with each adjacent cell rotated in the opposite direction. Mathematical modelling confirms that the formation of a dislocation cell structure assists in the process of energy minimization.

A proportionality has been cited by Kuhlmann-Wilsdorf with regard to the size of the dislocation cell, L, and the average dislocation link length l' [29]. In the relation

$$L = gl' \tag{4}$$

the proportionality constant g varies from 200 to approximately 14, depending on the material and the degree of work hardening. The usefulness of average link length is also found in the equation

$$l_S = 3l' \tag{5}$$

where l_S is the link length of a multiplying dislocation [2,29] . Kuhlmann-Wilsdorf has found that dislocations propagating from dislocation cell walls originate from the longest free dislocation link length. This link length is three times the average link length within the cell wall [25].

As dislocations multiply and emerge from cell walls, they enter dislocation free material and subdivide existing dislocation cells. The longest dislocations bow out, because they have the highest line energy and are most mobile. Cell subdivision is possible by the formation of cell walls by hierarchy [23]. New cell walls develop within the existing cells. New and old cell walls develop coincidentally. The "hierarchy" refers to the age, positioning, and smaller size of new cells.

The phenomena of dislocation cell shrinkage is explained by similitude and only occurs during stage II. Stage II begins when the formation of dislocation cells is

possible, and ceases when the dislocation cells reach a minimum size. Similitude is understood by the equation:

$$\tau - \tau_O = kGb(L^{-1}) \qquad (6)$$

where the cell size, L, is inversely proportional to the flow stress, τ, and the frictional stress, τ_O, is assumed to be negligible; k is a constant, G is the shear modulus, and b is the Burgers vector [2,23,30]. Under similar conditions (number of available slip planes, glide directions, mechanical stability) where k remains constant, twice the stress can be carried by a dislocation structure where the cells are half the size. Thus, the dislocation cell size decreases as the stress increases during stage II.

Cell size reduction and increased tolerance to stress are understood to be the significant attributes of stage II. The interdependence of these two attributes are shown by the principle of similitude, as described by the meshlength theory [2,29]. In summary, dislocations bow and multiply during straining. Increased dislocation density leads to shorter free link lengths of dislocations. Shorter link lengths require higher flow stress for mobility. Dislocation cells carry higher stresses as they shrink in size and the free link length decreases. Similitude of dislocation cells provides a comprehensive explanation of material behaviour during stage II.

2.2.3 Breakdown of Similitude

Stage III of work hardening appears when the near linear hardening of stage II approaches a quadratic curve. The end of stage II is marked by the breakdown of similitude. Possible causes for the demise of similitude have been identified by Kuhlmann-Wilsdorf [2]. One concern is the strength of the local dislocation arrangements within the cell walls. Should the dislocation arrangement within the cell

walls give way, possibly by excessive stress, the repercussions would be revealed by a change in the work hardening rate.

A second possible cause for the breakdown of similitude concerns the necessity of maintaining the lowest energy configuration available. If a new dislocation structure of lower energy that dislocation cells became available during stage II, this new structure would be favoured. A potentially radical change in dislocation arrangement would occur, depending on the dissimilarity between this new configuration and the existing cell structure. Accompanying the rearrangement would be a change in the work hardening rate.

Depletion of unstressed cell interiors is a probable cause for the breakdown of similitude. At the transition between stages II and III, the existing dislocation cells contain few stray dislocations. The cells are small enough that any stray dislocation is drawn into a cell wall to provide mutual stress screening [2]. An individual dislocation within a cell interior is unstable, because a lower energy state, provided by stress screening, is available in the cell wall. This reaction is inescapable due to the close proximity of the surrounding dislocation walls. Nucleation sites for new cell walls are provided by the interaction of dislocations within cell interiors. With clean cell interiors, dislocation cell size stabilizes and similitude ceases to operate.

2.2.4 LEDS in Stage III

Stage III of work hardening maintains a LEDS at constant size, as the strain is further increased. Cell walls continue to receive dislocations and cells continue to rotate relative to one another. The meshlength theory of Kuhlmann-Wilsdorf deals predominantly with stage I, the transition from stage I to II, stage II, and the transition from stages II to III. A detailed analysis of stage III is not provided. However, a near

parabolic curve with a slower work hardening rate than stage II is acknowledged for stage III by Kuhlmann-Wilsdorf [2,31]. It is presumed that the achievement of minimum cell size lessens the rate of dislocation density increase [32]. Dislocation cells experience rigid body rotation as the high dislocation density is concentrated in the cell walls [33].

Jackson addresses stage III of work hardening by applying the principle of energy minimization [34]. Jackson considers dislocation cell walls to be the load bearing structure of dislocation cell arrangements which are impenetrable barriers to individual dislocations. Localized plastic relaxation within cell walls may have one of two effects. If slip occurs on the primary slip system, dislocations within the cell walls annihilate, and dynamic recovery softens the material. Alternately, if slip occurs on the secondary slip systems, work hardening continues as the cell walls strengthen. The factor which dictates work softening or work hardening is the particular orientation of the cell walls with respect to the shear stress. The orientation for increased work hardening is unique; other orientations favour work softening, which supports the overall decreased work hardening rate of stage III.

The meshlength theory is based on the principle of energy minimization. The progression of low energy dislocation structures observed during the various stages of work hardening corresponds well with the dislocation configurations anticipated by Kuhlmann-Wilsdorf. Dislocation structures, driven to lower energy states by utilizing mutual stress screening, evolve into recognized LEDS as described by the meshlength theory. The stress screening mechanism, originally identified by Taylor, provides the incentive for the formation of cell walls and is also the key factor in causing the existence of a minimum dislocation cell size. The breakdown of similitude indicates the end of stage II. A lower rate of work hardening is a characteristic of stage III.

2.3 Stage IV of Work Hardening

At very large strains, a fourth stage of work hardening has been identified [12]. The large strains required to attain stage IV are obtained using torsion or compression tests, since tensile specimens usually fail at strains much less than that necessary for stage IV. Two factors indicative of stage IV are subgrain substructure and a further decrease in work hardening rate.

The subgrain substructure of stage IV is unlike the dislocation cells of stage III, though both are identified as low energy structures [12]. The cell walls in stage III are made up of many dislocations packed into areas of high dislocation density. The behaviour of dislocation cells is predictable using LEDS theory [23]. The substructure of stage IV reveals a sharp subgrain structure, and individual dislocations are not prevalent. The behaviour of subgrains formed by large straining is found to be similar to thermal subgrains [35].

It is proposed by Sevillano and Aernoudt [12] that initial subgrains form when dislocations move from cell interiors into cell walls and are annihilated. Dynamic annihilation of dislocations occurs at subgrain boundaries. The subgrain structure is the low energy substructure which evolves from LEDS in the range of strain much greater than unity (one). The shape of the subgrains, in the traverse direction of specimens, transforms from elongated shapes into equiaxed substructure at strains greater than four [12]. The formation of subgrains is the continuation in dislocation behaviour to seek minimum stored energy via the path of least resistance.

2.4 Classical Ductile Fracture

Severe plastic deformation is the distinguishing feature of ductile fracture [36]. Ductile fracture is a complex process involving several parameters. Propagation of a ductile crack requires a high degree of plastic flow ahead of the crack tip, and the crack propagates in a methodical step-wise fashion. By contrast, brittle fracture occurs rapidly. Energy required for cleavage (brittle fracture) breaks atomic bonds directly ahead of the crack tip, and is much less than the energy needed for plastic deformation associated with ductile fracture [9].

FCC and some BCC metals exhibit ductile fracture when subjected to sufficient uniaxial loading [9]. After initial elastic strain, localized plastic deformation occurs in the necked region of the tensile specimen. Necking is identified by a volume where further strain is concentrated [37]. Triaxial stresses result in the necked region, complicating the stress state [38]. Necking creates a stress concentration. Areas of high local stress, such as a necked region, are susceptible to accelerated local deformation [3]. Void growth is accelerated in the necked region of a tensile specimen undergoing ductile fracture [39]. Fracture inevitably occurs in the necked region.

Cup and cone fracture with microscopically dimpled fracture surfaces occur in metals with inherent particles, such as precipitates, second phase particles and inclusions. The formation of a cup and cone fracture begins with stress concentrations at the inclusion sites in the necked region. Voids initiate at these sites and grow with continued applied stress. Coalescence of voids produces the fracture surface. Local stress states determine the macroscopic fracture surface shape. Ductile fracture initiated at particles is described in the following paragraphs.

Void initiation at particle sites has been observed in numerous studies [40,41,42]. The particle-matrix interface is particularly prone to high stresses and strains because of the difference in elastic modulus of the hard particles and ductile matrix. Void initiation at particle sites has been modelled in several studies. Argon et al. [43] have chosen stress as the critical parameter indicative of void initiation. Their work relates local elastic energies and interfacial strength to cavity formation for equiaxed inclusions of various sizes. Goods and Brown [44] use critical strain, rather than stress, to determine void initiation. Their work shows a dependence between critical strain and particle size. Void initiation mechanisms include particle fracture and particle-matrix interface separation, among others. Finally, an energy approach is adopted by Fischer and Gurland [45,46] which uses a double criteria of elastic energy release and critical normal stress. This model provides a list of material characteristics which encourage void nucleation. Some factors which assist void initiation are large particle size, low work of adhesion, high flow stress, and location of particles on grain boundaries. Modelling approaches vary, but void initiation at particle sites is a well established concept.

Experimental observation provides evidence of particles at void initiation sites. Puttick [41] tested tough pitch copper in tension and found voids originated at inclusions by either decohesion or inclusion fracture. He also observed void growth in the necked region where triaxial stresses and strains are present. Broek [47] provides a comparison between dimple size and inclusion spacing in aluminum alloys. Void initiation at large second phase particles (10 μm or larger) were observed at small strains, however these voids were not found to be as critical to the fracture process as voids initiated at smaller particles. Broek presented a one to one correspondence between average spacing of small particles and average dimple spacing. Thus, dimples were deemed to have formed from voids which originated at small particles.

Particle shape and orientation are discussed by Goods and Brown [44]. Equiaxed particles generally give way to particle matrix decohesion. Whereas, elongated particles are prone to cracking. The frequency of particle cracking increases as the long axis of a particle approaches the tensile axis [48]. Elongated particles consistently crack in their mid-section. This observation is explained by fiber loading theory [49]. The tensile stress in a fiber builds from the ends towards the middle; maximum tensile stress is at the fiber (or elongated particle) midsection. Other theories for particle cracking, such as a dislocation pile-up mechanism, do not predict particles cracking at their midsection [44].

Void growth and coalescence leads to final fracture, as ligaments between the voids rupture. Voids in copper elongate in the longitudinal direction of the tensile specimen [50]. Brown and Embury [42] provide a geometric explanation of void growth and coalescence in copper. Void growth in the longitudinal direction is believed to be by plastic extension. Void coalescence begins when the void lengths approximate the intervoid spacing. At this point, glide planes may operate between the voids. The ligaments thin and rupture, completing the fracture process.

The final fracture surface shape of a cylindrical tensile specimen, at the macroscopic level is known as "cup and cone". The fracture surface of one end of the broken specimen resembles a cup and the other a cone, as shown in Figure 2.2. Both surfaces have a flat central region, perpendicular to the tensile axis. Both surfaces have a conical periphery, creating the "cup" and "cone" distinction [50].

Two mechanisms for void growth and coalescence are described by Bluhm and Morrissey [51] which account for the flat central region and conical periphery of cup and cone fracture surfaces. The inclined shear lip is exposed to biaxial stress, while the macroscopically flat central portion of the fracture surface endures triaxial stresses. Bluhm and Morrissey have combined this information with experimental observation.

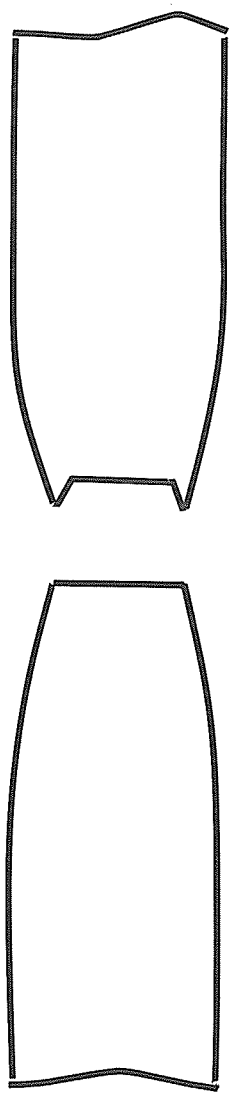

Figure 2.2: Cup and Cone Fracture Surfaces

(Figure from Reference[50].)

Voids in the shear lip coalesce by linkage, as the material in the band shears. Voids in the central region coalesce as the material between the voids behaves like miniscule tensile specimens [9]. The strain produced by these small regions of necking is negligible compared to the gross deformation which has already occurred. The different dimple shapes in these two regions are indicative of the type of void coalescence at final separation.

The macroscopic fracture surface of pure single crystals is different than the standard cup and cone fracture surface often associated with ductile fracture. High purity metals which fail in ductile fracture often have a knife edge fracture surface [9]. These metals deform by pure slip. Mobile dislocations are not obstructed by particles and are able to glide freely. Dislocations are expelled at the edges of the crystal. Extensive slip causes the metal to taper, producing the knife edge. Final rupture is pure slip between atomic planes.

Other macroscopic fracture surface shapes resulting from ductile fracture include necking to a point and bands of localized deformation following the fracture surface. However, the cup and cone fracture surface is the most widely recognized.

2.5 Dislocations and the Ductile Fracture Process

There is substantial evidence which indicates dislocation cell walls serve as void initiation sites and microcrack paths during tensile failure of high purity metals. Material failure by rupture is common and indicates continuous ductility, as it requires 100% reduction in area. Microscopic aspects of rupture include microvoids and severe slip.

Investigations of ductile fracture identify the formation of microcracks ahead of a propagating crack as it traverses through the necked portion of a tensile specimen

[4,32,33,52]. Two significant attributes of microcracks are initiation in regularly spaced distances ahead of the crack and formation in material volumes which have become hard locally.

Microcracks have been observed to form ahead of a propagating crack at regular spacings of 0.5 μm for silver [32] and 2-4 μm for aluminum-copper crystals [53,54]. The regular submicron-size spacing is a curiosity. It is too small and regular to be explained by traditional void initiation mechanisms. Void initiation at second-phase particles are not the cause, since no such inclusions were found in the microcrack region in an investigation by Lyles [52]. Precipitates are also found to have little influence on microvoid formation from in-situ electron microscope observations and post-fracture studies by Chan and Wilsdorf [54]; interface decohesion at precipitates does not necessarily create a regular series of microvoids.

A comparison of void density and particle density by Bauer and Wilsdorf [55] reinforces the lack of correspondence between microvoids and particles. Intervoid and interparticle distances were measured. The average void density was found to be 100 times greater than the average particle density. Decohesion at particle interfaces alone could not be responsible for the multitude of voids. Another striking observation is increase in void density with applied stress [55]. Such a relationship suggests dislocation density is a key factor in void initiation. Bauer and Wilsdorf concluded that voids in excess of the particle density were initiated at vacancy clusters or microvoids.

Cracks in a work hardening material propagate through a volume of material which has become hard locally and is least ductile. Extensive plastic deformation precedes fracture in ductile materials, often involving dislocation densities in the order of 10^{11} and 10^{12} dislocations per cm^2 [32]. Heavily work hardened areas contain dislocation

structures. The walls of dislocation cells are potential sites for microvoid initiation, due to the high dislocation density.

The large quantity and submicron size of dislocation cells fits with the microvoid observations. The spacing of microvoids ahead of a crack is of the same order of magnitude as dislocation cell size. The spacing of microvoids has been observed to vary between 0.2 and 0.5 μm, as previously stated. Minimum dislocation cell size was found to be 0.4 μm in the present study (Chapter 4) and 1.0 μm in a study by Pollock and Wilsdorf on beryllium [56]. The similar sizes of dislocation cells and microvoid spacing, in general, is noteworthy.

It is the energy available at dislocation cell walls which make them potential sites for microvoid initiation. New dislocations, generated in stage III, contribute to cell rotation. The energy at the cell boundary increases during cell rotation [33]. The energy required for fracture or decohesion across an interface is given as:

$$W_F = 2\gamma_S - \gamma_B \qquad (7)$$

where W_F is the work of fracture, γ_S is surface free energy, and γ_B is surface energy of the interface [4]. Cell rotation increases γ_B at cell walls. Therefore, cell walls are energetically favoured sites for microvoid initiation.

Critical evidence for microvoid activity at cell walls is supplied by Pollock and Wilsdorf [56]. Their study of beryllium single crystals revealed in-situ observations of microcrack initiation, as well as crack propagation, along dislocation cell walls. The first cell structures were observed in the region of a crack tip caused by a stress concentration (required for in-situ observation). The most developed cells were always in that region, due to continuous cell development. Formation, subdivision, and rotation of dislocation cells were observed during tensile straining. The first microvoid appeared suddenly. It occurred on a cell boundary oriented parallel to the plane of the existing crack.

Subsequent microcracks were also on cell boundaries parallel to this plane. Microvoid propagation was considerably slower than initiation. Microvoids grew by plastic deformation, thinning ligaments of material between them. Additional microvoids and highly rotated dislocation cells were observed in thinning ligaments. Final separation was achieved by shear on a single glide system within a cell or by more complicated rupture.

The works of Pollock and Wilsdorf [56] and others [4,33] illustrate the role of dislocation cell walls during microvoid initiation and growth in a material free of precipitate particles. The lack of precipitate particles and, therefore, the ability to omit particle interface decohesion as a cause for void initiation is significant. The involvement of dislocation cells in the fracture process places more importance on the understanding of dislocation cell behaviour during work hardening.

Post-failure analysis of ductile fracture specimens by Klassen [57] gives evidence of dislocation cell-sized dimples on fracture surfaces. HSLA tensile specimens were pulled to failure. The minimum dislocation cell size (end of stage II work hardening) was measured and compared to the fracture dimple size. The two measurements were of the same order of magnitude, suggesting interdependence.

A model for crack propagation in a work hardening material is provided by Bassim [58]. This model identifies mobile dislocation density, which is reflected in the degree of dislocation cell development, as the key parameter in determining the ability of an advancing crack tip to blunt. Three cases are cited. The first case deals with low dislocation density, such as an annealed state. The low density does not provide enough dislocations for blunting action at the crack tip, and fracture toughness is low.

Crack tip blunting is achieved in case two, when the mobile dislocation density is high and dislocation structures have not formed. These mobile dislocations are free to interact with the crack tip. Their abundance provides significant ability for blunting. Dislocations which do not interact with the crack tip are drawn into newly forming dislocation structures.

The third case involves high dislocation density and well defined dislocation structures. Few dislocations are able to interact with the crack tip, since dislocation cells are approaching their minimum size, and any new dislocations are drawn into the cell walls. The lack of dislocations available for crack tip blunting causes low fracture toughness, as was found in case one. The crack propagates through a region of dislocation walls.

Dislocation cell walls provide sites for microvoid initiation and propagation during ductile fracture. Microvoids initiate in regularly spaced intervals which are in the same order of magnitude as minimum dislocation cell size. In-situ electron microscope observations have shown cracks travelling along high energy dislocation cell walls of favourable orientation, by microvoid initiation and coalescence. Post-fracture analyses and crack path models provide further support for microvoid initiation and propagation at dislocation cell walls.

3. EXPERIMENTAL PROCEDURE

Cylindrical tensile specimens of commercial copper were used for a variety of tests in this research project. Copper rod stock was machined into cylindrical tensile specimens. These specimens were pulled to failure in tension. The broken tensile specimens were later sectioned to provide samples for microscopic examinations and analyses.

3.1 Specimen Preparation

Tensile specimens were machined and heat treated before tensile testing. Grain size and inclusion content measurements were taken. A diameter profile was made of each broken specimen half.

3.1.1 Machining

Commercial purity copper rod stock of 12.70 μm (0.050 inch) diameter was machined into threaded end cylindrical tensile specimens in accordance with ASTM Specification E8-85a [59]. The specimens had a gauge length of 25.40 μm (1.00 in) and a gauge diameter of 5.35 μm (0.25 in). The tensile specimen is shown in Figure 3.1.

3.1.2 Heat Treatment

Two grain sizes and three crosshead speeds were used to obtain six different classes of specimens. Two grain sizes were obtained by using two heat treatments. All specimens were annealed in an argon atmosphere at 620 °C for two hours and furnace cooled. An argon atmosphere was provided by encasing each specimen in Pyrex glass

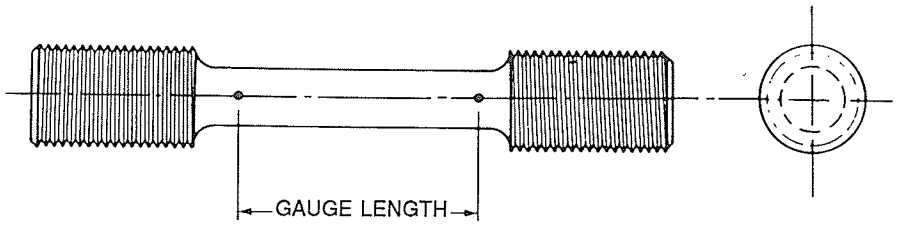

GAUGELENGTH: 2.54 cm
DIAMETER OF GAUGE LENGTH: 1.27 cm

Figure 3.1: Cylindrical Tensile Specimen

tubing and replacing the air in the encasement with argon gas. All specimens were plastically prestrained to 10% engineering strain. Half of the specimens were subsequently heat treated at 404 °C in an argon atmosphere for one hour and air cooled. The other half of the specimens were processed similarly with a heat treatment temperature of 608 °C.

3.1.3 Grain Size Measurement

The resulting grain sizes were determined using Jefferies' planimetric method [60]. This method required an etched surface with grain boundaries revealed. The etchant used was 5 g $Fe(NO_3)_3$, 25 ml HCl, and 70 ml water. Grains wholly within the circle and grains intersecting the circle circumference were counted, using a Vickers Instruments Fifty-Five Microscope with 75X magnification and a face plate with a standard 79.8 mm (3.1 in) diameter hole. Jefferies' formula provided a value for average number of grains per square area. Since the grains were equiaxed, the simple equation of the area of a circle was used to convert grains per square millimeter to average grain diameter in millimeters.

3.1.4 Inclusion Measurement

Inherent to commercial copper was the presence of inclusions. The average inclusion diameter and nearest neighbour spacing were found in the cross sectional plane. A Leitz image analyzer was used to measure inclusion diameter. Equivalent diameter values were calculated based on the area of the inclusions, as determined by digitized images of the polished specimen surface. The nearest neighbour spacing of the inclusions was determined by the radial distance between an inclusion and the inclusion

closest to it. The distance was measured from inclusion center to inclusion center using a Nikon Epiphot-TME optical microscope with a calibrated eyepiece.

3.1.5 Mechanical Testing

Tensile testing was carried out on an Instron 1137 screw-driven tensile test rig. Constant crosshead speeds were used for all tensile tests. Nominal strain rates were calculated subsequently. Crosshead speed and nominal strain rates are listed in Figure 3.2. Data was sampled automatically by an IBM XT personal computer and saved on hard disk. The data sampling rate was dependent upon the crosshead speed. The two parameters sampled were force and crosshead position. Force was read from a load cell (rated at 150 kg), and the crosshead position was read from a linear variable displacement transducer attached to the Instron 1137 frame. From these two parameters, along with the original specimen dimensions, the following and other pertinent parameters were calculated: engineering stress, engineering strain, true stress, and true strain. A standard chart recorder was also used, in case any computer data was inadvertently lost.

3.1.6 Diameter Profiles

Diameter profiles of the broken halves of the tensile specimens were taken. Vernier calipers were used to measure axial distance from the gauge point and the diameter at that location, as shown in Figure 3.3. The profiles were graphed in the form of reduction in area versus distance from the gauge point. This information was paramount when the work hardening characteristics were related to the amount of plastic strain sustained.

Crosshead Speed (mm/min)	Nominal Strain Rate (s^{-1})
0.80	3.90×10^{-4}
0.44	2.14×10^{-4}
0.08	0.39×10^{-4}

Figure 3.2: Crosshead Speeds and Nominal Strain Rates

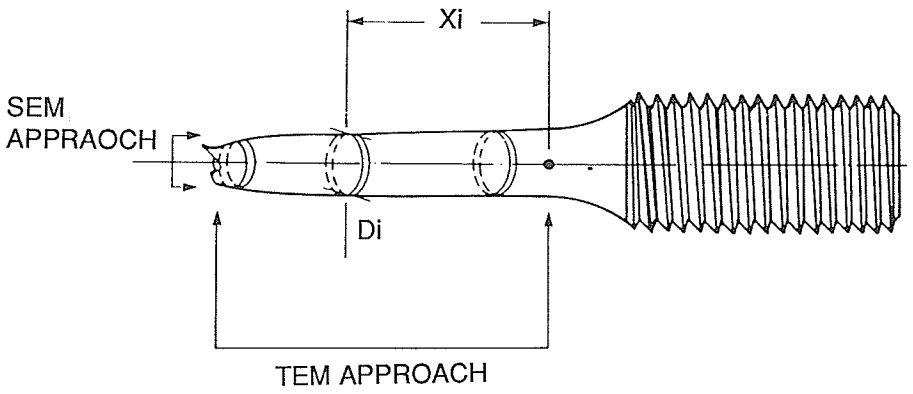

Figure 3.3: Klassen Sectioning Technique to Produce SEM and TEM Samples

3.1.7 Specimen Sectioning Technique

The broken halves of the tensile specimens were sectioned following the procedure developed by Klassen [57,61]. The fundamental advantage of this method is the production of sections of constant reduction in area. Figure 3.3 shows a sectioned specimen. The fracture end of the specimen was examined using scanning electron microscopy, to study the fracture process and for chemical analysis of inclusions. Transmission electron microscopy and microhardness testing were performed on sections of the specimen progressively farther from the fractured end, which had decreasing values of reduction in area.

The full potential of the Klassen sectioning technique, as applied to cylindrical tensile specimens, was found in the correlation of data obtained from a single broken tensile specimen. Ideally, it should be possible to reconcile the mechanisms of plastic deformation determined from transmission electron microscopy with the fracture mechanisms determined from scanning electron microscopy. This was the case for the HSLA steels studied by Bassim et al. [62] where dimple size was correlated with minimum dislocation cell size. It was the objective of this present study to pursue the possibility of a similar correlation in copper, hence the Klassen technique of specimen sectioning was applied.

3.2 Measurement of Fracture Surface Dimple Size

Determination of dimple size on the fracture surface required the use of a scanning electron microscope (SEM) and an image analyzer. Image processing steps used to measure the dimple size are illustrated in Figure 3.4 and summarized as follows:

1) SEM micrographs of the dimpled fracture surface were taken;
2) the outlines of the dimples were traced by hand onto clear plastic sheets;
3) the tracings were digitized;
4) the digitized images were automatically measured to obtain equivalent diameter and mean chord length.

Samples for SEM were easily obtained by slicing off the fracture surface from the broken tensile specimens with a 0.31 mm (0.012 in) thick diamond grit wheel on a Buehler ISOMET 11-1180 low speed saw. The fracture surfaces were photographed at 1000X magnification in a JEOL JXA-840 scanning electron microscope. Micrographs of the dimples were obtained, even though focussing was aggravated by the 45° incline of the fracture surface.

The dimples were traced by hand onto clear plastic sheets which were used as specimens to measure dimple size. The dimple shapes were digitized using a Leitz image analyzer. Images to be analyzed were always crisp and unobstructed using this technique. The image analyzer has a selection of inherent functions and measurable parameters from which a program was written to perform the required measurements.

The area of a dimple and the diameter of a circle of the same area were used to determine equivalent diameter. To calculate mean chord length, three intermediate measurements were required. The image analyzer measured the width of the digitized image projected in three directions and averaged the readings, to produce the mean chord length. Approximately 120 traced dimples were measured for each parameter value.

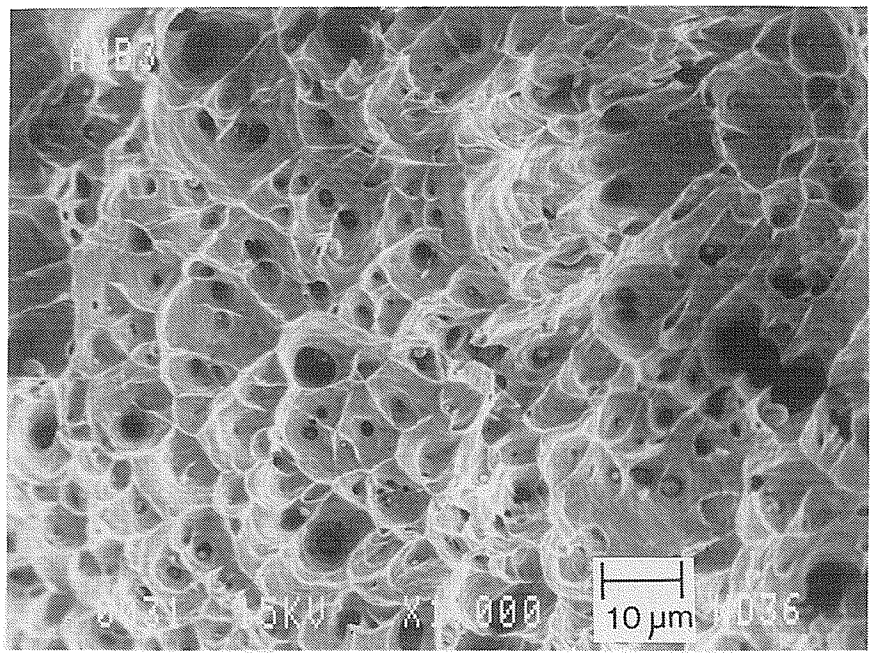

(a)

(b)

Figure 3.4: Dimple Measurement Technique

(a) SEM Micrograph of Dimpled Fracture Surface
(b) Digitized Dimple Shape

Specimen Class: 50.0 µm Grain Size; 3.90×10^{-4} s^{-1} Strain Rate

3.3 Measurement of Dislocation Cell Size

Dislocation cell size measurements required preparation of transmission electron microscope (TEM) foils. Foils were cut and thinned using standard techniques.

3.3.1 Sectioning of Tensile Specimens

Tensile specimen halves were sectioned perpendicular to their tensile axis using the same diamond wheel which was used to remove the fracture surface, to provide samples for TEM observation. The specimen halves were sectioned into 0.33 mm (0.013 in) thick slices by progressively moving the 0.31 mm (0.012 in) thick cutting blade in increments of 0.64 mm (0.025 in). Typically, a weight of 100 grams and a speed setting of 5 was used; each slice took approximately 20 minutes to cut. The reduction in area of each slice was known, since the distance from the gauge point was known and the diameter profile had been previously determined.

The slices, initially 0.33 mm (0.013 in) thick, were hand polished to a thickness of 0.13 mm (0.005 in) using grit paper and polishing wheels with diamond paste grit. To create thin discs suitable for electropolishing, 3 mm (0.012 in) diameter discs were punched out of the thin slices using a small metal punch and hammer. One slice provided just one disc. The concern of disturbing existing dislocation structures by the process of punching discs was abated, by comparing the observations of TEM foils prepared by the punch method and by the method of spark erosion. Spark erosion does not involve gross plastic deformation. No discrepancy was found in the specimens prepared by the two methods.

3.3.2 TEM Foil Making Conditions

Electropolishing of the thin 3 mm (0.12 in) diameter discs was performed on Streurs Tenupol-2 electropolishing equipment with an electrolyte of 15% nitric acid and 85% methanol. A caution warning exists for this electrolyte [63]; it is not to be stored. Fresh electrolyte was made for each session of electropolishing. Preparation of thin foils had the highest success rate at the following conditions: 1.0 - 1.8 amperes, 22 volts, -30 °C, and a flowrate setting of 4. Once a hole was detected, the foils were washed in methanol twice to remove the electrolyte and then once in ethanol for a final rinse.

3.3.3 Photographing Dislocation Cells

Two transmission electron microscopes were used during the study, a JEOL 2000FX STEM and a Philips EM-300 TEM. Accurate representation of dislocation cells requires the correct operating technique of a transmission electron microscope. To ensure that the dislocation cells were not incomplete or misrepresented, the specimen was positioned so that the diffraction pattern was acceptable before an area was photographed.

TEM imaging is based on diffraction of the incident beam by the crystal lattice of the specimen. Different images may be produced by the same set of atoms by changing the tilt angle of the crystal lattice with respect to the incident beam. To correctly represent the dislocation cells on the TEM viewing screen, the lattice structure was orientated such that as many dislocations as possible were visible simultaneously. It is recognized that all twelve burger vector orientations of an FCC cubic structure cannot be visible simultaneously, but as many burgers vector orientations as possible were made visible simultaneously. This was achieved by adjusting the foil so that the diffraction pattern included the largest number of operative reflections and the intensity of these

reflections was uniform over the viewing screen. This adjustment was made by tilting the foil with respect to the incident electron beam. The JEOL 2000FX TEM has a two-axis tilt specimen holder to facilitate this operation.

After the optimal diffraction pattern was found, the TEM was switched into image mode. Finally, the dislocation cells were photographed after minor optical adjustments. All dislocation cell micrographs were taken at X20K magnification.

3.3.4 Dislocation Cell Size Measurement

The measurement of average dislocation cell diameter was made from the TEM micrographs directly. Dislocation cells usually formed in rows. This was convenient for the purpose of cell measurement. Using the linear intercept method, the length of a row of dislocation cells was measured to obtain the average diameter of the dislocation cells in that row [64]. Several micrographs were taken of each TEM foil to provide statistical variation of the average dislocation cell size. Approximately 200 cells were measured for each data point. The dislocation cell sizes were plotted against reduction in area for each of the six specimen classifications.

3.4 Microhardness Measurements

Two different sets of microhardness data were obtained. One set was used to determine the variation of microhardness with respect to reduction in area, and the second set was used to determine relative strength of grain boundaries and grain interiors. The two microhardness tests shared the same samples.

3.4.1 Average Microhardness

The tensile specimen halves were sectioned in a manner similar to the production of TEM foils to provide microhardness samples. Again, the advantage of exposing an area of constant reduction in area was made possible by the specimen sectioning technique of Klassen. For microhardness, the tensile specimen halves were sectioned into 1.35 mm (0.053 in) chunks which were mounted in black bakelite moulds. The samples were highly polished so that crisp microhardness indentations would be made. The reduction in area value for each microhardness sample was determined by noting the distance of each cut of the diamond grit wheel from the gauge point of the tensile specimen half, and using the previously obtained diameter profile of that particular tensile specimen half.

A 200 gram load applied for 10 seconds was used for the average microhardness measurements. At least five indentations, or 10 readings, were made for each sample. The data was plotted in the form of microhardness versus reduction in area for the six different specimen classifications.

3.4.2 Microhardness of Grain Interiors and Grain Boundaries

To determine the relative strength between grain interiors and grain boundaries, the microhardness samples were repolished and tested again using a substantially lighter load. Microhardness values for grain interiors required an indentation size considerably smaller than the grain. The copper used in the present study also contained twinning which further restricted the indentation size. A 2 gram weight was used to produce indentations small enough to fit into a grain or twin interior with ample margin. Only those indentations which landed entirely within the confines of a twin interior and at least

one indentation width from any grain or twin boundary were accepted for grain interior readings.

To measure the microhardness of a grain boundary, the size of an indentation would ideally be in the order of the size of the grain boundary itself. Practically, however, measurement of microhardness of a grain boundary relied on approximation, since the microhardness indentation also fell on grain interior material. Only those indentations which landed fairly well centered on a grain boundary were accepted as grain boundary readings.

Since the objective of the 2 gram microhardness testing was to confirm higher microhardness in grain boundaries compared to grain interiors, it was not necessary to correlate microhardness readings to the reduction in area values, as was done for the 200 gram microhardness test. In all, 24 grain interior measurements and 23 grain boundary measurements were used. Each microhardness measurement involved eight readings.

4. EXPERIMENTAL RESULTS

The experimental results of this study were conclusive and provided information necessary to define the development of dislocation cells in commercial purity copper during tensile plastic deformation. The most conclusive result illustrating dislocation cell development is a curve depicting dislocation cell size as a function of reduction in area. The experimental results also provide information about fracture mechanisms involved in the failure of copper tensile specimens. Results from auxiliary tests reinforce the chief findings.

4.1 Material Properties

Material properties were determined prior to dimple size and dislocation cell size measurements. The microstructure, chemical composition and mechanical properties were evaluated.

4.1.1 Microstructure

Optical examination of the copper showed a heavily twinned grain structure speckled with inclusions. Etched cross sections revealed equiaxed grains as shown in Figure 4.1. The two grain sizes were found to be 42.5 μm and 50.0 μm (average diameter).

The inclusion distribution was similar for the two grain sizes. The inclusions were near circular in cross section and were grouped in loose clusters throughout the material. The 42.5 μm grain material had inclusions with an average diameter of 0.972 μm and an average nearest neighbor spacing of 13.5 μm. The 50.0 μm grain material had

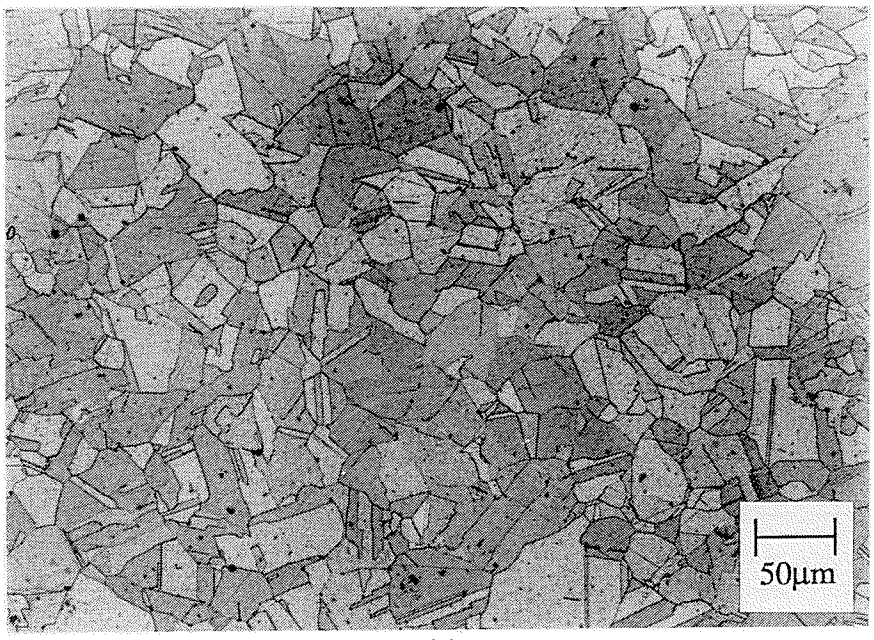

(a)

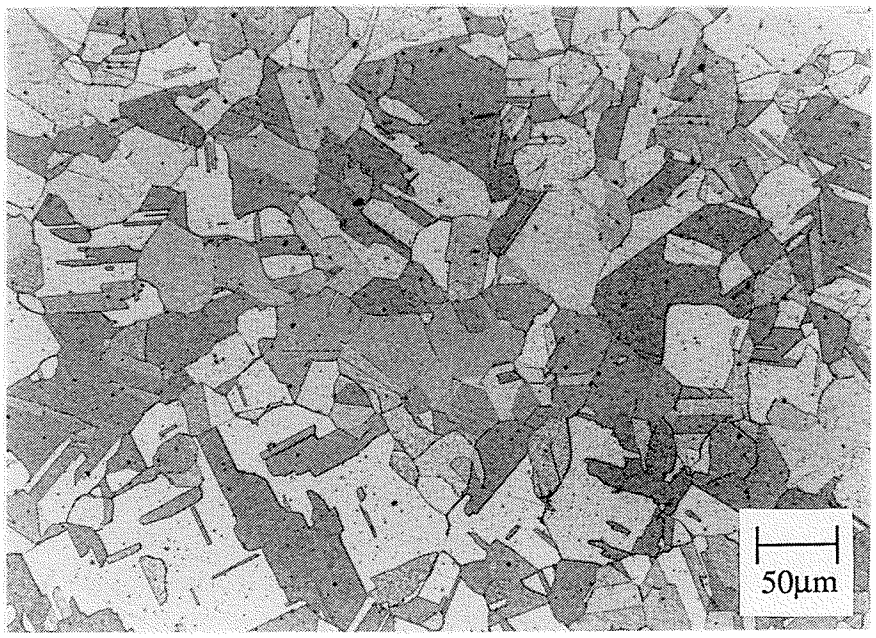

(b)

Figure 4.1: Etched Cross Sections

(a) 42.5 μm Grain Size
(b) 50.0 μm Grain Size

inclusions with an average diameter of 0.842 μm and an average nearest neighbor spacing of 13.7 μm.

In this thesis, all examinations and analyses of the copper tensile specimens were performed using cross sections. For this reason, characterization of the microstructure in the longitudinal direction was not essential. However, the microstructure in the longitudinal direction contained elongated grains and elongated inclusions. The longitudinal direction was the rolling direction for rod stock during manufacture.

4.1.2 Chemical Composition

The chemical composition was typical of commercial copper. Common alloying elements for copper include aluminum, silicon, beryllium, and cadmium [65]. It was likely that these elements would be present in commercial purity copper. As determined by EDX examination performed on the JEOL JXA-840 scanning electron microscope, the inclusions contained aluminum and silicon. The result of an EDX examination of an inclusion is shown in Figure 4.2. The copper peaks in Figure 4.2 were caused by the background matrix of copper. Bulk chemical analysis performed by Arrow Laboratory Incorporated confirmed the EDX results. Figure 4.3 shows the chemical analysis of the commercial copper.

4.1.3 Material Properties

Stress-strain diagrams and various parameters were determined from the load-displacement data collected during the tensile tests. Figure 4.4 summarizes the mechanical properties calculated. Finer grain size is associated with higher strength, and there is no pronounced effect due to strain rate. The values in Figure 4.4 are typical of commercial purity copper [21,66].

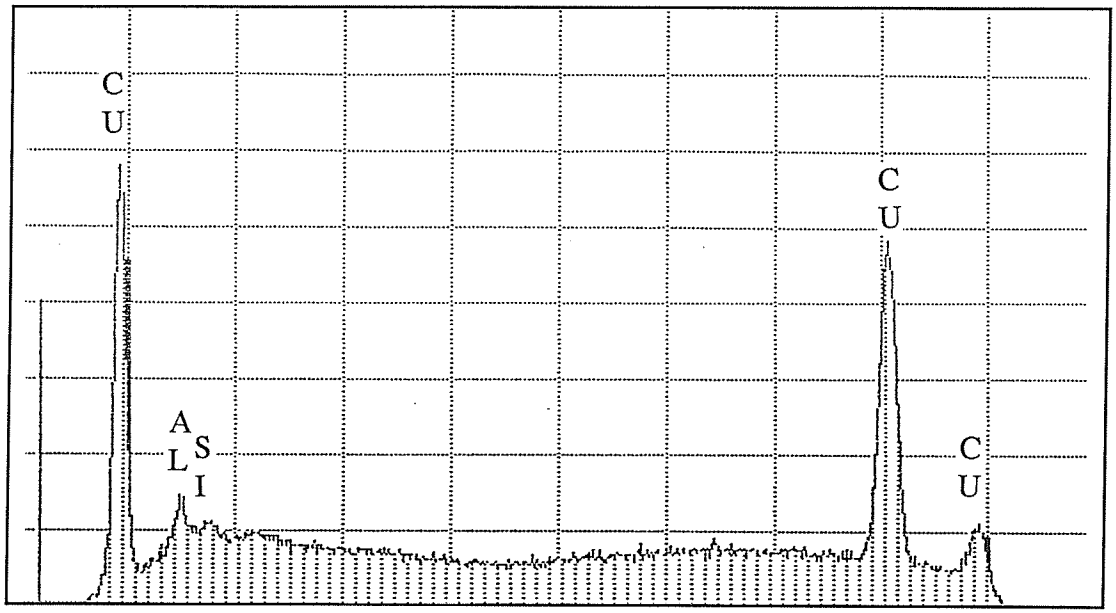

Figure 4.2: EDX Analysis of a Typical Inclusion

Element	Percentage (weight)
COPPER	99.94
ALUMINUM	<0.01
SILICON	<0.005

Chemical analysis performed by Arrow Laboratory, Inc., Wichita, Kansas

Figure 4.3: Chemical Analysis of Commercial Copper

Specimen Classification		Yield Stress (MPa)	Maximum Strain (%)
Grain Size (μm)	Nominal Strain Rate (10^{-4} s^{-1})		
42.5	3.90	57.86	42.42
50.0	3.90	23.69	49.27
42.5	2.14	36.77	45.88
50.0	2.14	23.47	47.07
42.5	0.39	47.75	45.43
50.0	0.39	20.11	51.90

Figure 4.4: Mechanical Properties of Tested Specimens

The strain rate sensitivity exponent values were expected to be less than 0.10 and were found to be consistently less than 0.03. The strain rate sensitivity exponent values were found to be of the correct order of magnitude for tests performed at room temperature [37]. There was no significant difference in strain rate sensitivity between the two sets of grain sizes.

The stress-strain curves for the copper tensile specimens were characteristic of a work hardening material. Engineering stress-strain curves exhibited a smooth arc up to the point of maximum load, after which necking and final fracture of the specimen accompanied a rapid fall in engineering stress. True stress-strain curves were constructed up to the point of maximum load (tensile instability) by converting from engineering stress and strain to true stress and strain. Figure 4.5 shows a representative true stress-strain curve for one of the specimens tested. The conversions between true stress and strain and engineering stress and strain are given below,

$$\sigma = s(e+1) \tag{8}$$

$$\varepsilon = \ln(e+1) \tag{9}$$

where σ is true stress, ε is true strain, s is engineering stress and e is engineering strain.

The strain hardening exponent was calculated using two methods. The first method determined the strain hardening exponent at the point of tensile instability. The point of tensile instability is generally indicated by the condition of maximum load [37]. It has been shown mathematically [37] that at the point of tensile instability, the value of true uniform strain is equal to the value of the strain hardening exponent. Therefore, the strain hardening exponent was found by observation, using a true stress-strain diagram.

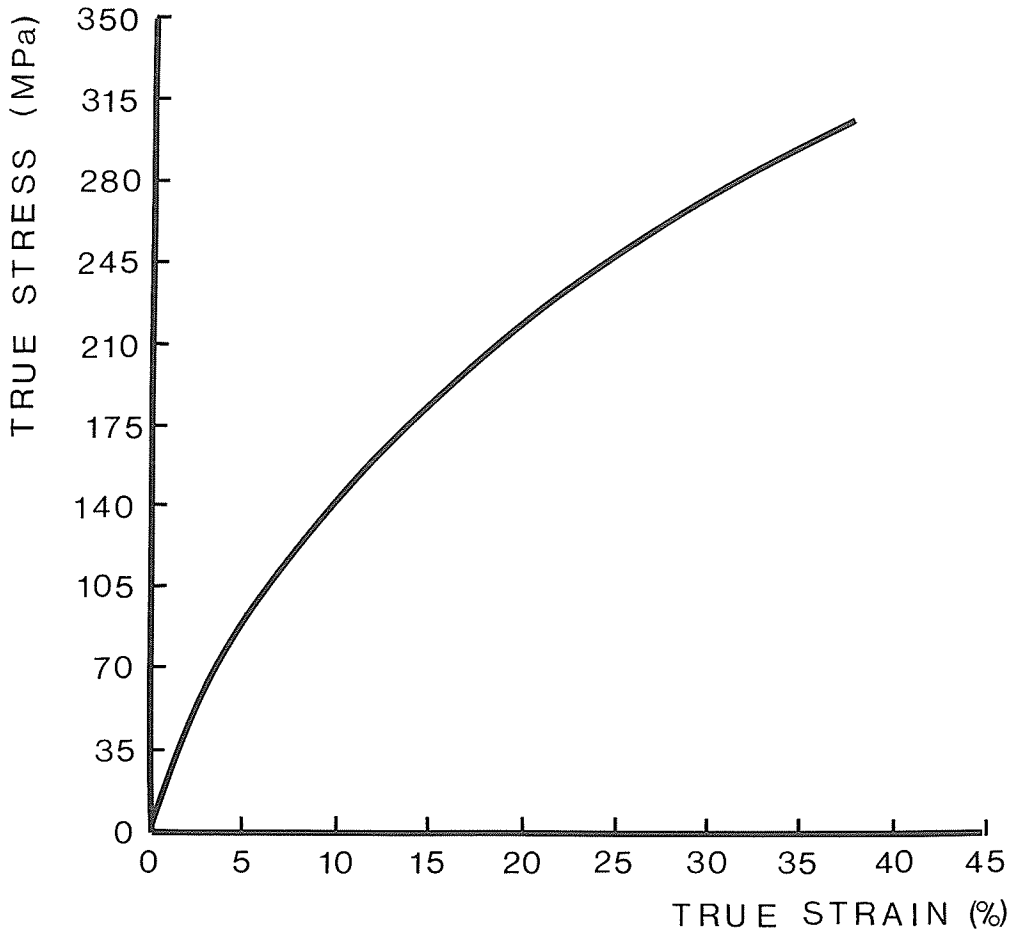

Figure 4.5: True Stress-Strain Curve for Tested Copper Specimen

Specimen Class: 42.5 μm Grain Size; 3.90×10^{-4} s^{-1} Strain Rate

The second method for determining the strain hardening exponent used the equation of the flow curve. A flow curve is assumed to be mathematically represented by the equation

$$\sigma = K\varepsilon^n \qquad (10)$$

where K is the strength coefficient, n is the strain hardening exponent, and σ and ε are true stress and true strain respectively. Plotting the flow curve on a log-log scale revealed the value of the strain hardening exponent as the slope of the line. The values for the strain hardening exponent as calculated by these two methods compared well with reference values; see Figure 4.6.

4.2 Fracture Surface

The macroscopic shape and the microscopic texture of the fracture surfaces were examined.

4.2.1 Shape of Fracture Surface

The tensile specimens fractured after exhibiting necking, and all specimens fractured in the necked area. All of the tensile specimens, except one, produced similar fracture surface shapes. The fracture surfaces consisted of several planar faces inclined at approximately 45° from the tensile axis. The one exception was a single shear plane fracture surface inclined at 45° from the tensile axis.

Specimen Classification		n (true strain at ultimate stress)	n (graphical method)
Grain Size (μm)	Nominal Strain Rate (10^{-4} s^{-1})		
42.5	3.90	0.37	0.53
50.0	3.90	0.44	0.69
42.5	2.14	0.40	0.57
50.0	2.14	0.42	0.66
42.5	0.39	0.40	0.56
50.0	0.39	0.47	0.66

Reference [37] shows annealled copper to have a strain exponent, n, of 0.54.

Figure 4.6: Strain Hardening Exponent Values

4.2.2 Texture of Fracture Surface

By SEM examination, the topography of the fracture surfaces was shown to be dimpled. The dimples were either self-enclosed or cascading, depending on their location on the tensile cross section. Figure 4.7 is a line diagram depicting the two basic shapes. The cascading dimples were difficult to categorize and were not used for dimple measurements.

Dimples used for measurement were located near the center of the specimen cross section and were well defined as shown in the SEM micrographs, Figure 4.8. The dimples were contiguous and not necessarily circular. The boundaries of the dimples were defined by walls of metal which tapered to a thin edge. For the most part, inclusions were seated in the dimples. Dimples rarely contained more than one inclusion.

The dimples were measured using two parameters, namely equivalent diameter and mean chord length. These two parameters were similar and exhibited parallel trends even though the numerical values differed. On average, the values of equivalent diameter were 29% larger than the mean chord length. Figure 4.9 gives equivalent diameter and mean chord length values for the six specimen classifications.

Discrimination of dimple size, based on grain size or strain rate, did not prove to be significant. However, the material with slightly larger inclusion size also had slightly larger dimple size; refer to Figure 4.9. The correspondence between inclusion size and dimple size was reinforced by closer examination of the fracture surface topography. On each specimen surface, the size of the dimple was proportional to the size of the resident inclusion. Note in Figure 4.8 that large dimples were associated with large inclusions and smaller dimples contained smaller inclusions. Dimple size was observed to be

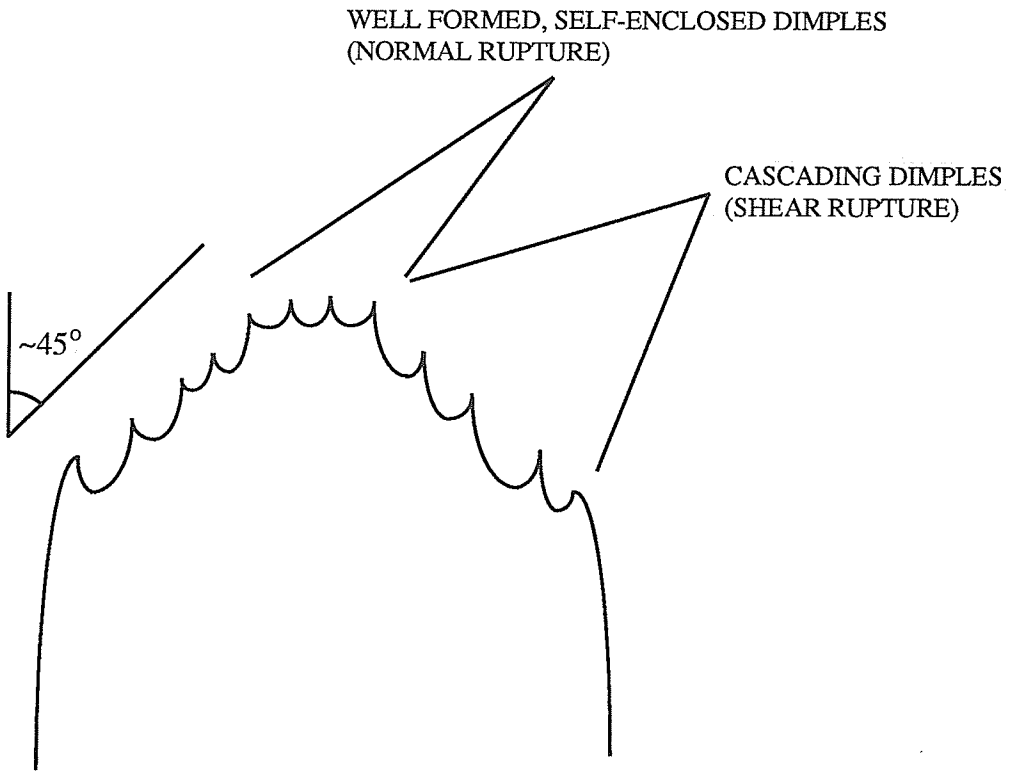

Figure 4.7 Exaggerated Shape of Dimples on Fracture Surface from Side View

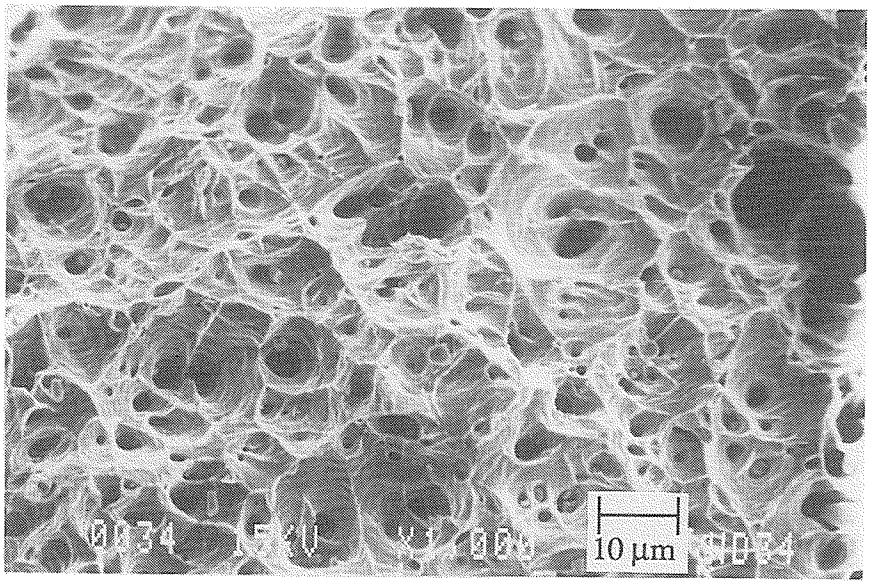

(a)

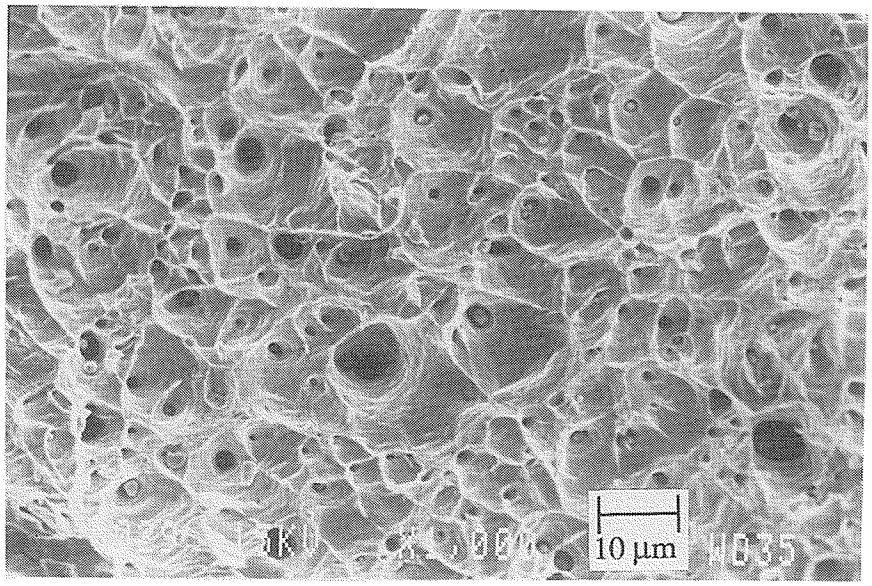

(b)

Figure 4.8: Fracture Surface Dimples

(a) 42.5 µm Grain Size; 3.90×10^{-4} s^{-1} Strain Rate
(b) 50.0 µm Grain Size; 3.90×10^{-4} s^{-1} Strain Rate

CONTINUED ON NEXT PAGE

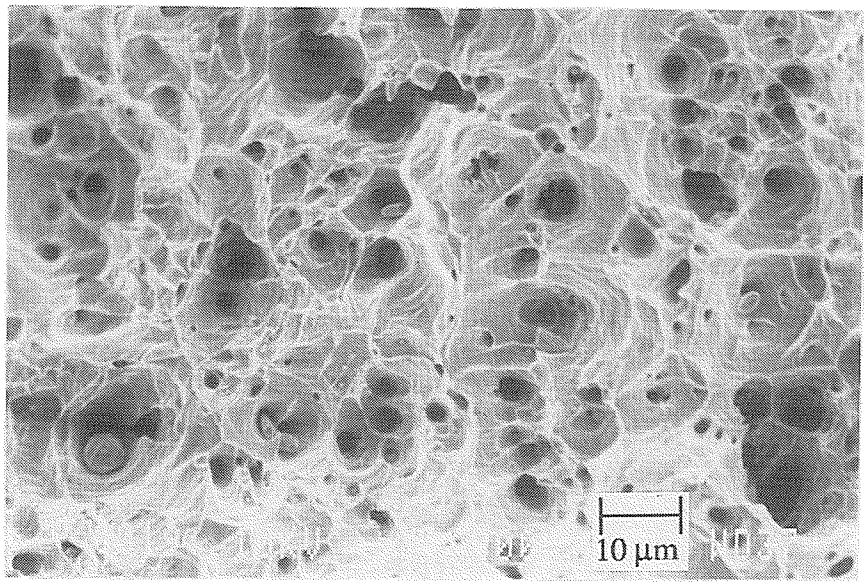

(c)

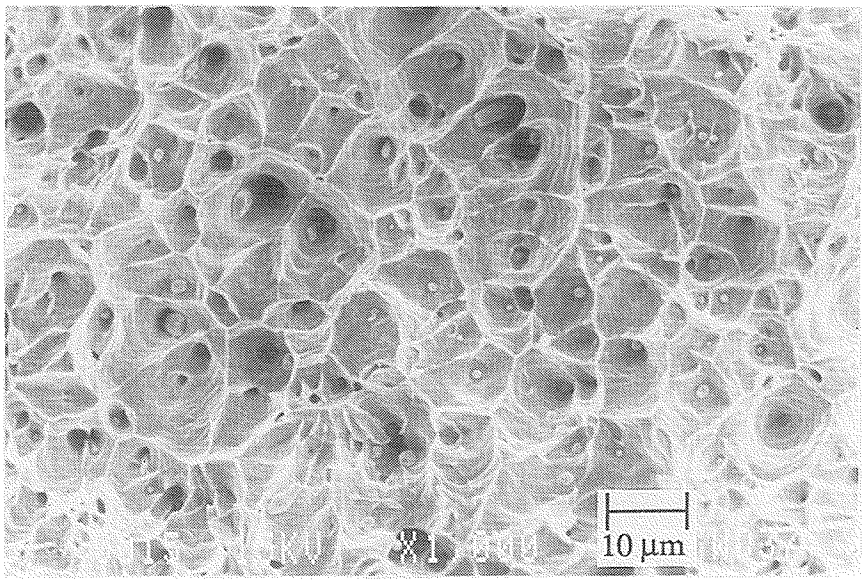

(d)

Figure 4.8: Fracture Surface Dimples

(c) 42.5 µm Grain Size; 2.14×10^{-4} s^{-1} Strain Rate
(d) 50.0 µm Grain Size; 2.14×10^{-4} s^{-1} Strain Rate

CONTINUED ON NEXT PAGE

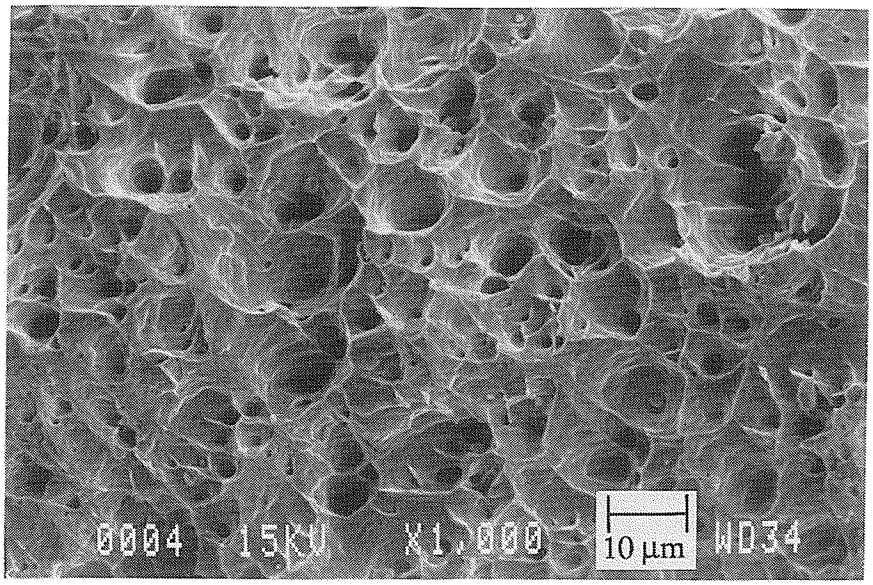

(e)

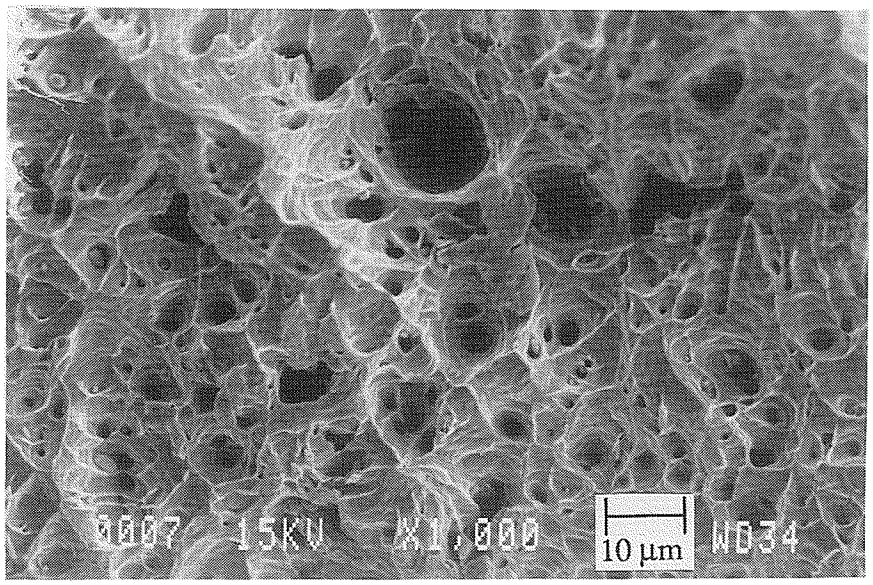

(f)

Figure 4.8: Fracture Surface Dimples

(e) 42.5 µm Grain Size; 0.39×10^{-4} s^{-1} Strain Rate
(f) 50.0 µm Grain Size; 0.39×10^{-4} s^{-1} Strain Rate

Specimen Classification		Equivalent Diameter (μm)	Mean Chord Length (μm)
Grain Size (μm)	Nominal Strain Rate (10^{-4} s^{-1})		
42.5	3.90	6.77 +/- 0.49	4.82 +/- 0.36
50.0	3.90	6.24 +/- 0.42	4.40 +/- 0.30
42.5	2.14	6.73 +/- 0.52	4.81 +/- 0.40
50.0	2.14	6.61 +/- 0.36	4.66 +/- 0.26
42.5	0.39	6.85 +/- 0.42	4.74 +/- 0.29
50.0	0.39	6.51 +/- 0.36	4.65 +/- 0.27

Figure 4.9: Dimple Size Measurements

proportional to resident inclusion size and was restricted by the existence of neighbouring dimples.

4.3 Dislocation Observation

The primary objective of TEM observation was to measure dislocation cell size Auxiliary observations, such as void initiation and grain size effect on dislocation cell size, were also noted.

4.3.1 Dislocation Cells

Cross sections of the cylindrical tensile specimens were used to make TEM thin foils for examination of dislocation structures. The repetitive pattern revealed was dislocation-free regions isolated from each other by areas of high dislocation density. The pattern was recognized as a dislocation cell structure. The dislocation cells did not form over the entire thin area of the TEM foils. The dislocation cells were present in patches.

The cell size, cell shape, and the structure of the cell walls varied with respect to the amount of strain incurred. A series of TEM micrographs of dislocation cells at different strains are shown in Figure 4.10. Strain was represented by the measurable parameter of reduction in area. Reduction in area is proportional to strain. In the foils which experienced relatively low strain (least reduction in area), the cell walls were relatively broad in width and loose in structure. By observing the TEM foils sequentially, in order of increasing reduction in area, evolution of the dislocation cells was revealed.

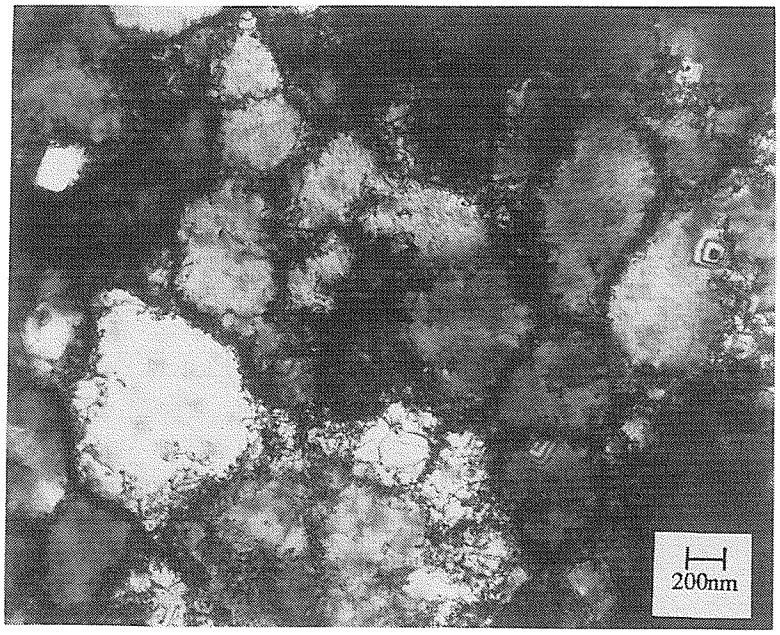

(a)

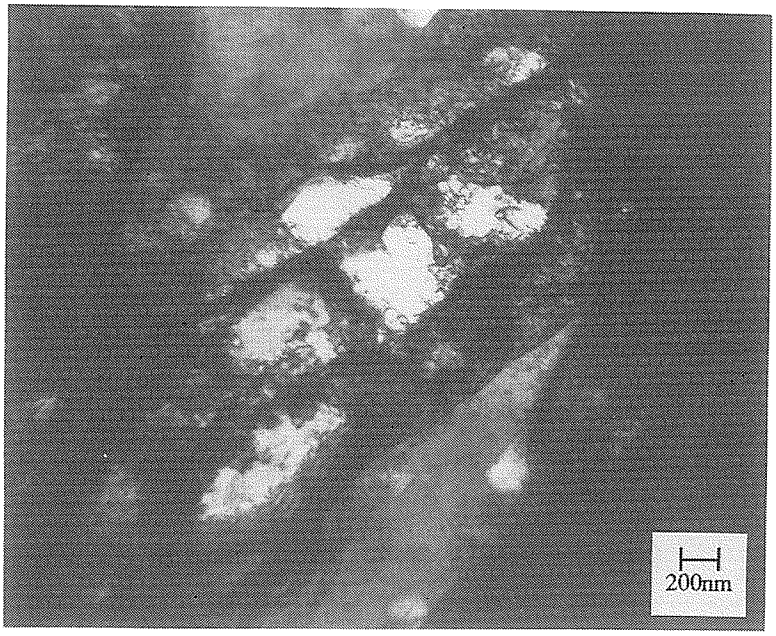

(b)

Figure 4.10: Development of Dislocation Cell Walls

(a) 31.3% Reduction in Area
(b) 36.2% Reduction in Area

Specimen Class: 42.5 μm Grain Size; 0.39×10^{-4} s^{-1} Strain Rate

CONTINUED ON NEXT PAGE

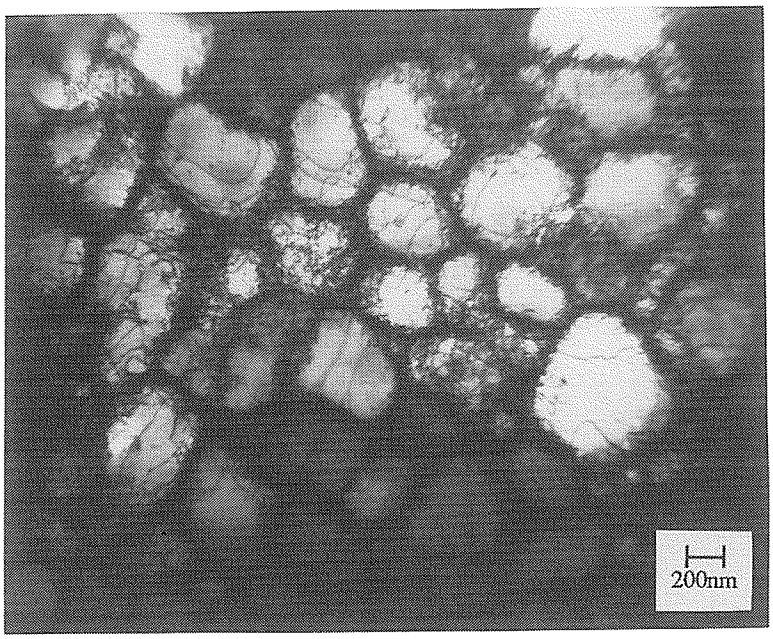

(c)

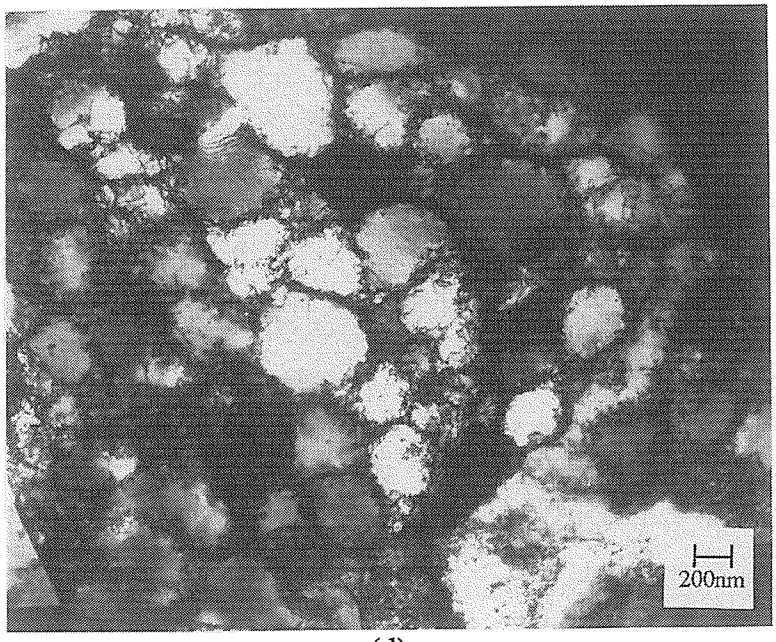

(d)

Figure 4.10: Development of Dislocation Cell Walls

(c) 40.3% Reduction in Area
(d) 50.2% Reduction in Area

Specimen Class: 42.5 μm Grain Size; 0.39×10^{-4} s^{-1} Strain Rate

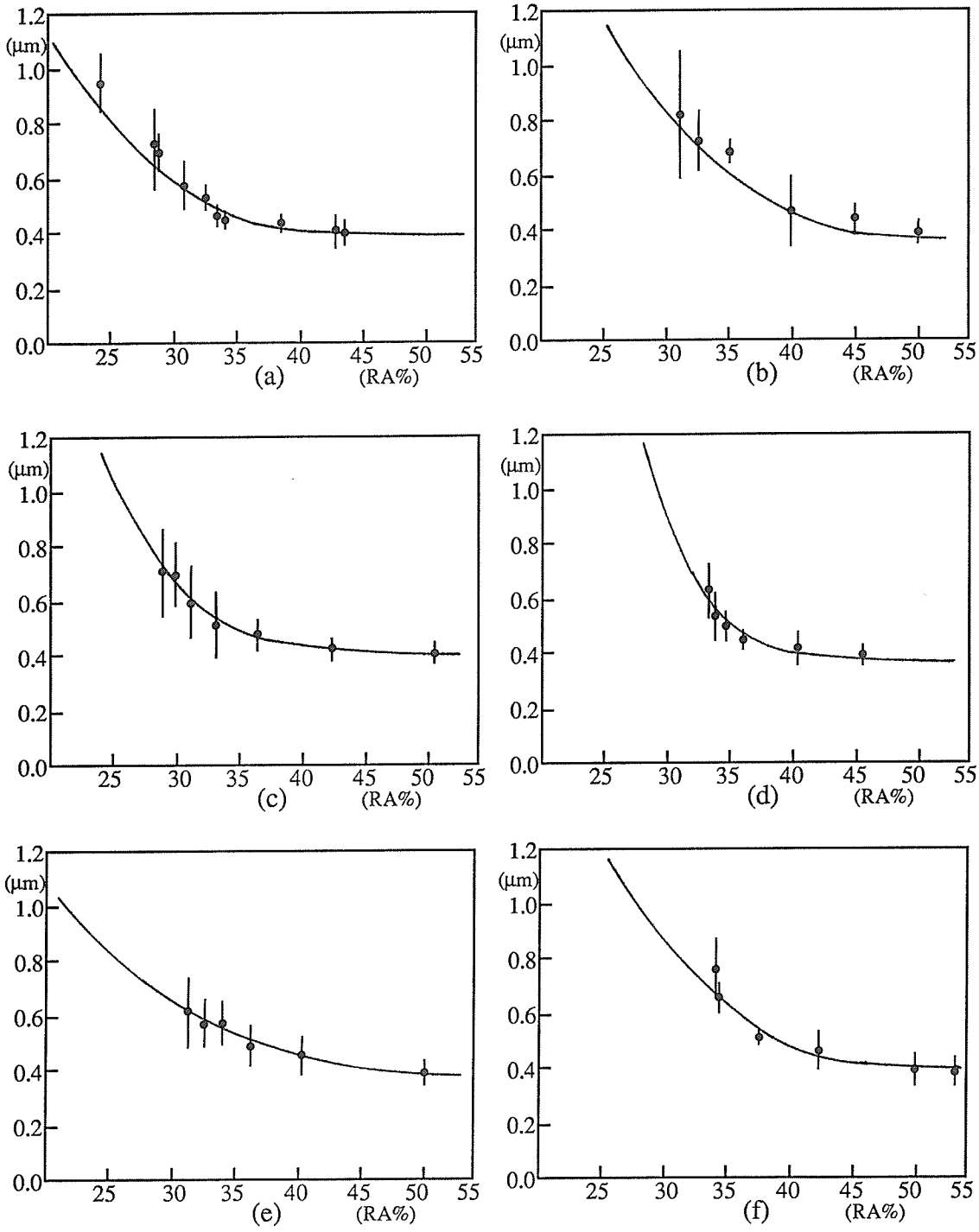

Figure 4.11: Dislocation Cell Size versus Reduction in Area Curves

(a) 42.5 μm Grain Size; 3.90×10^{-4} s^{-1} Strain Rate
(b) 50.0 μm Grain Size; 3.90×10^{-4} s^{-1} Strain Rate
(c) 42.5 μm Grain Size; 2.14×10^{-4} s^{-1} Strain Rate
(d) 50.0 μm Grain Size; 2.14×10^{-4} s^{-1} Strain Rate
(e) 42.5 μm Grain Size; 0.39×10^{-4} s^{-1} Strain Rate
(f) 50.0 μm Grain Size; 0.39×10^{-4} s^{-1} Strain Rate

Four noticeable trends developed as the reduction in area increased. Firstly, the size of the dislocation cells decreased monotonically as reduction in area values increased. The decrease in cell size occurred at a high rate up to a reduction in area value of approximately 35%. Beyond 40% reduction in area, the cell size became nearly constant. The minimum cell size was consistently found to be 0.4 μm. This trend was common to all six tensile specimen classifications, as shown in Figure 4.11.

The second trend of dislocation cell evolution involved the quantity of dislocation cells observed with respect to the amount of strain incurred; strain was expressed in terms of reduction in area. A marked increase in quantity and visibility of dislocation cell structures accompanied the increase in strain. Dislocation cell observation was facilitated by the large quantity of patches of dislocation cells in foils of higher reduction in area values.

The third trend dealt with the definition of the cell walls. The cell walls became crisper in definition as the reduction in area values increased. Specifically, the dislocation density increased and the walls became narrower. The dislocation density was too high to measure, and remained a qualitative observation. The narrowing of the dislocation cell wall width also remained a qualitative observation, but one with definition, as given below.

The dislocation cell walls associated with the lowest values of reduction in area were loose and were often accompanied by stray individual dislocations. At the other extreme, thin foils with the highest values of reduction in area showed dislocation walls so thin and sharp that they were deemed to be subgrain boundaries. The dislocation walls of mid-range reduction in are values depicted the transition with definite improvement in dislocation cell wall definition with increase in strain. In TEM foils with the highest values of reduction in area, subgrains boundaries were observed in addition to dislocation

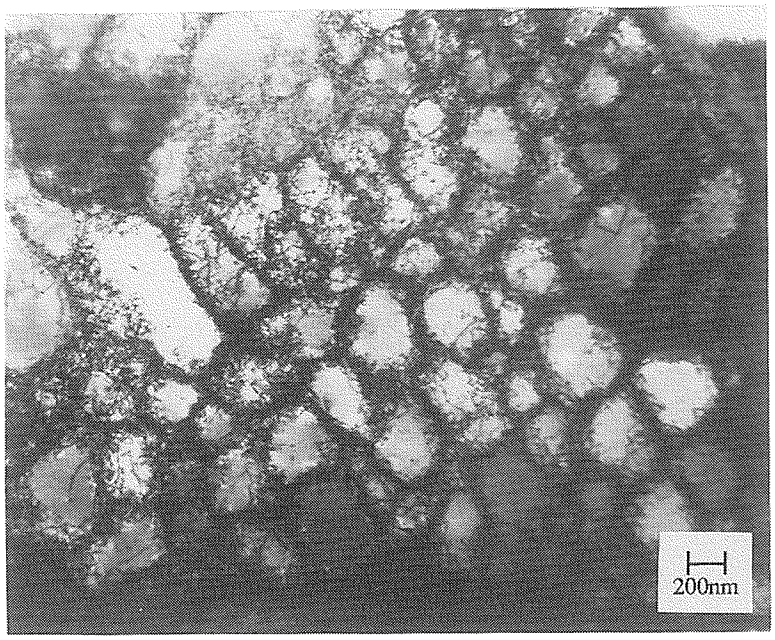

(a)

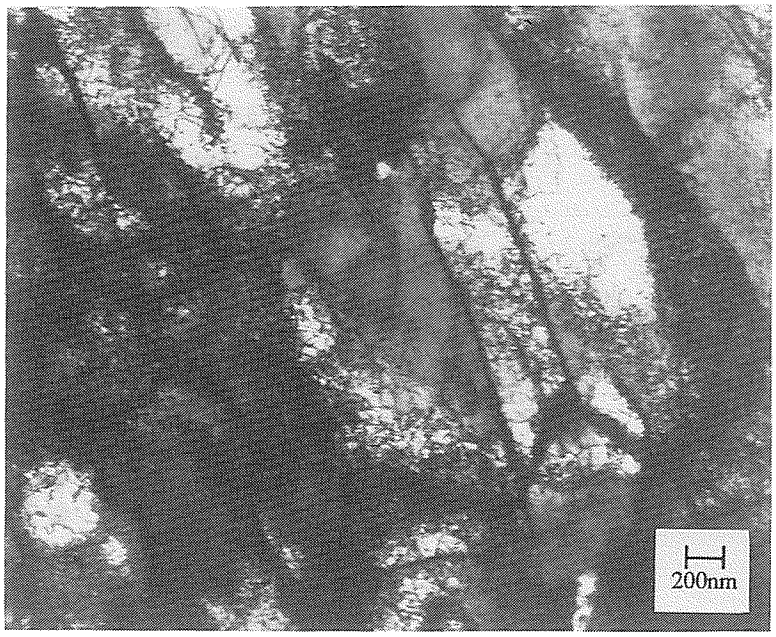

(b)

Figure 4.12: Subgrain Formation at High Strain

(a) Dislocation Cells At 43.0% Reduction in Area
(b) Subgrains at 41.5% Reduction in Area

Specimen Class: 42.5 μm Grain Size; 3.90×10^{-4} s^{-1} Strain Rate

cells. Figure 4.12 depicts subgrain boundaries found after minimum cell size had been reached.

The final observable trend was associated with the shape of the dislocation-free areas during the conversion of dislocation cell structure to subgrain structure. At 40% reduction in area, minimum dislocation cell size was achieved. The dislocation-free areas of dislocation cells were circular or near circular in shape in all specimens with less than 40% reduction in area. It was observed that dislocation cell walls frequently converted into subgrain boundaries at reduction in area values beyond 45%. The subgrains were elongated and usually included sharp angles, unlike the circular dislocation cells. This transition in shape of dislocation-free areas was abrupt rather than gradual. In the TEM foils of high reduction in area values, well defined dislocation cells and subgrains were found simultaneously. The difference in shape of dislocation-free regions was poignant.

A review of the observations made concerning the evolution dislocation cells includes:

1) Dislocation cell size decreased as strain (reduction in area) increased. Cell shrinkage ceased and a minimum cell size of 0.4 μm emerged after 40% reduction in area.

2) The number of patches of dislocation cells increased as reduction in area increased.

3) Dislocation cell wall definition improved and wall width narrowed as cell size decreased.

4) Dislocation cells were circular or near circular in shape. Subgrains were elongated in shape.

These trends were found to be true for all six classifications of tensile specimens. These observations were made using the parameter of reduction in area as a basis for

comparison. Reduction in area was also used as a reference parameter in previous works [61,67,68] and has proven to be a reliable unit of measure.

4.3.2 Supplemental TEM Observations

In addition to the TEM observations regarding the evolution of dislocation cells, two other TEM observations were noted. One was a rare and fortunate find made during operation of the transition electron microscope. Observation of dislocation cells by TEM involved roaming around the thin foil in order to find an area thin enough to allow the electron beam to be transmitted, as well as exposing the microstructure of interest. Usually, inclusions situated in the very thin edge around the hole of the foil fell out during specimen preparation, washing or handling. Evidence of their existence was a proliferation of holes in the foil other than the central hole. On one occasion, an inclusion remained imbedded in the thin foil and was clearly visible. Figure 4.13 shows this inclusion and the interaction of it with nearby dislocations. As shown in Figure 4.13, the interface between the inclusion and the copper matrix was cluttered with dislocations to the extent that a void was visible on one side of the inclusion. The interface between inclusion and copper matrix exhibited dislocation pile-ups and void initiation by decohesion.

The second supplemental observation was that grain size affected initial dislocation cell size. The larger grain material had larger initial dislocation cells. Comparison was made at the same reduction in area values for tensile specimens tested at the same crosshead speed (nominal strain rate), but with different grain sizes. The difference in cell size diminished as the cells became smaller. The minimum dislocation cell size was consistently 0.4 μm for all specimens. Figure 4.14 illustrates the effect of initial grain size on dislocation cell size. Using low reduction in area values as a basis for

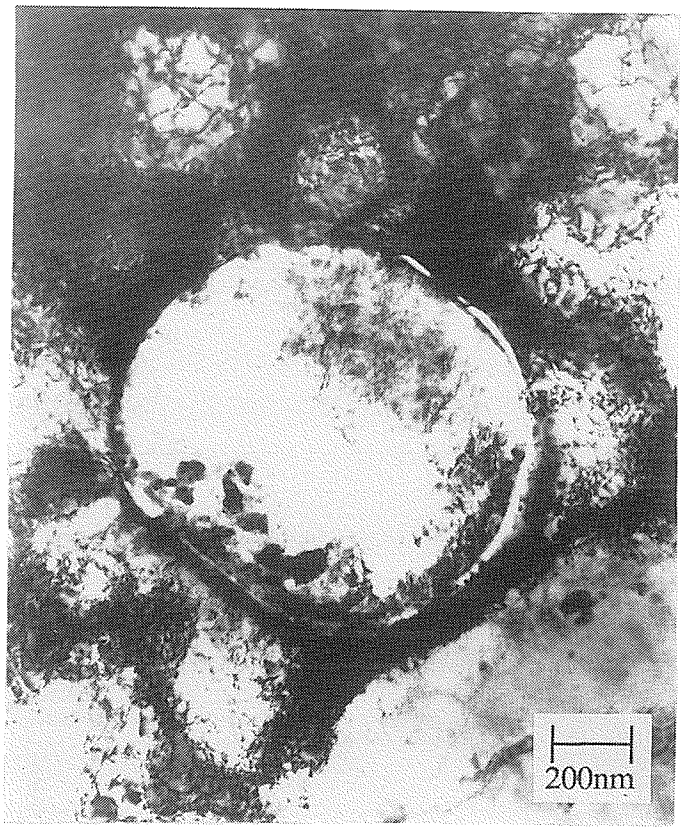

Figure 4.13: Void Initiation at Inclusion-Matrix Interface

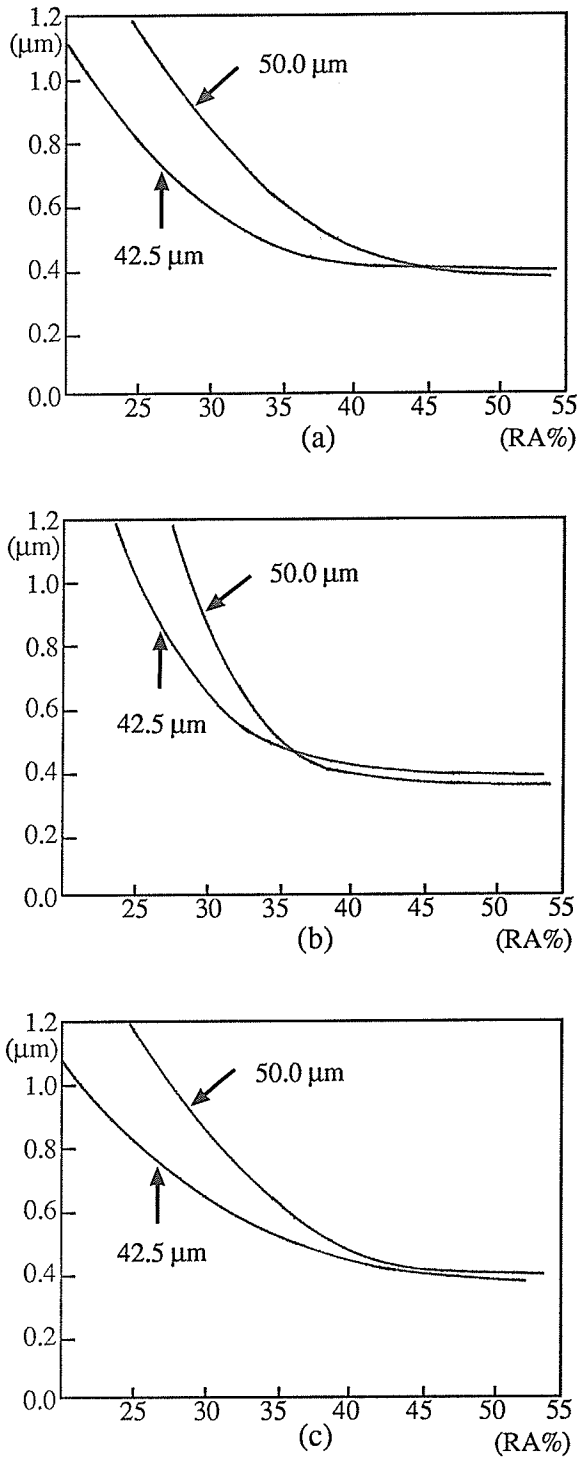

Figure 4.14: Effect of Initial Grain Size on Dislocation Cell Size

(a) 3.90×10^{-4} s^{-1} Strain Rate
(b) 2.14×10^{-4} s^{-1} Strain Rate
(c) 0.39×10^{-4} s^{-1} Strain Rate

comparison, tensile specimens of larger grain size produced larger dislocation cells compared to the tensile specimens of finer grain size. The difference in dislocation cell size became less apparent as the cells approached the minimum size.

4.4 Microhardness

Microhardness measurements were made to determine average hardness as a function of reduction in area and the relative hardness between grain boundaries and grain interiors.

4.4.1 Average Microhardness

Microhardness measurements were plotted against reduction in area for each of the six specimen classifications. Microhardness values represent the average microhardness of the specimen at a particular value of reduction in area. The microhardness curves, Figure 4.15, exhibit monotonic hardening as reduction in area values increase, up to approximately 37% reduction in area. Beyond 37% reduction in area, the microhardness curves continued to show increase with reduced slope.

4.4.2 Grain Interior and Grain Boundary Comparison

A 2 gram microhardness test was used to determine the relative hardness of grain boundaries and grain interiors. The microhardness values were similar for the different specimen classifications. On average, the microhardness of the grains interiors and grain boundaries were characterized by a 6.0% difference, with the grain boundaries exhibiting higher microhardness.

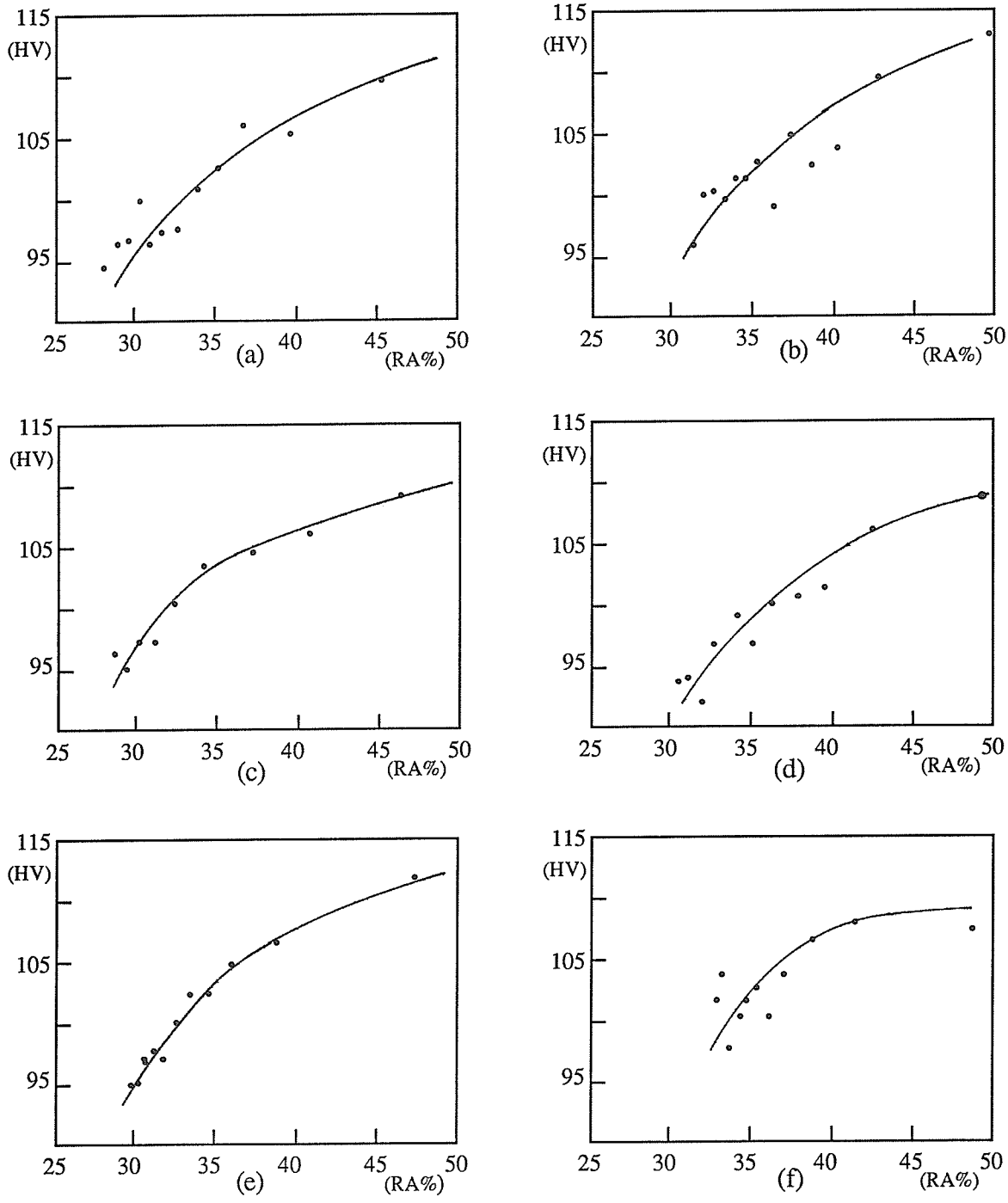

Figure 4.15: Microhardness versus Reduction in Area Curves

(a) 42.5 μm Grain Size; 3.90×10^{-4} s^{-1} Strain Rate
(b) 42.5 μm Grain Size; 2.14×10^{-4} s^{-1} Strain Rate
(c) 42.5 μm Grain Size; 0.39×10^{-4} s^{-1} Strain Rate
(a) 50.0 μm Grain Size; 3.90×10^{-4} s^{-1} Strain Rate
(b) 50.0 μm Grain Size; 2.14×10^{-4} s^{-1} Strain Rate
(c) 50.0 μm Grain Size; 0.39×10^{-4} s^{-1} Strain Rate

4.5 Diameter Profile

Correlation of dislocation cell size measurements and microhardness measurements to reduction in area values required diameter profiles for each specimen. Diameter profiles provided the link between two standards of reference. Data was measured in terms of distance from gauge point, but required in terms of reduction in area. Thus, the reference for cell size or microhardness was converted from distance from gauge point to reduction in area.

Diameter profiles showed uniform specimen deformation, except for the necked region where there was severe localized deformation. Figure 4.16 shows a typical curve of reduction in area versus distance from the gauge point for a broken tensile specimen half.

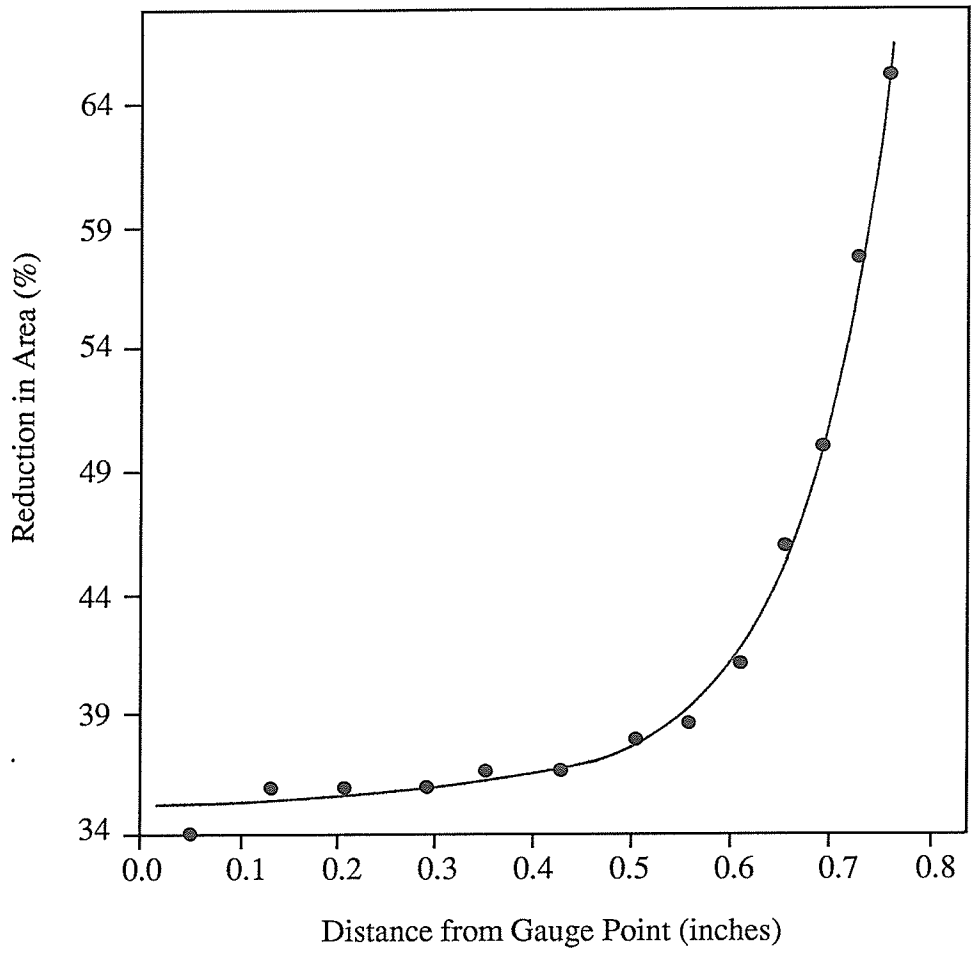

Figure 4.16: Typical Diameter Profile Curve

5. DISCUSSION OF RESULTS

The present study characterized dislocation cell development in commercial copper subjected to tensile testing. Observed interactions of dislocations agreed with the meshlength theory of work hardening by Kuhlmann-Wilsdorf. Also, mechanisms involved in the fracture process of the copper tensile specimens were identified.

5.1 Evolution of Dislocation Structures During Deformation

Dislocation cell development was observed in the range of reduction in area values studied. Similitude and hierarchical formation of cells were evident. Subgrain formations were identified after minimum cell size was attained.

5.1.1 Existence of Dislocations Cells and Similitude

Dislocation cells were the LEDS observed in commercial copper tensile specimens. A consistent pattern of dislocation cells was found in all specimens examined in the present study. Dislocations formed equiaxed cells, which approximated the cell structure with minimum energy originally proposed by Bassim [28]. Figure 4.10 shows dislocation cells observed in the present study. The cells evolved from loose tangles into distinctive entities.

Similitude is the reduction in size of LEDS due to increase in flow stress. The dependence of dislocation cell size on low stress during similitude is given by Equation (6), Section 2.2.2. The dislocation cell pattern in the present study retained its geometric shape and became smaller as stress and strain increased. The dislocation cells exhibited similitude, as shown in the cell size versus reduction in area curves, Figure 4.11. The

smaller cells were induced by higher flow stress, in accordance with stage II behaviour described by the meshlength theory of work hardening. The dislocation cells studied existed at high values of stress and strain, near the point of fracture. Similitude was observed up to approximately 40% reduction in area.

The dislocation cell size data obtained at high stresses preceding failure were compared to data from a similar study of polycrystalline commercial copper tested in tension [69]. The two independent sets of results compared favourably, as shown in Figure 5.1. Data from the previous study showed a graphical trend of decreasing dislocation cell size with increasing shear stress. Dislocation cell measurements taken in the present study extend the trend into a higher stress region, close to the fracture point. The dependence of average dislocation cell size on shear stress was found to be continuous. Similitude is shown to be active from the formation of the earliest dislocation cell patterns through to the minimum dislocation cell size for polycrystalline commercial copper.

5.1.2 Cell Wall Definition

As similitude took place, the dislocation cells became smaller in size and the dislocation cell walls became narrower and better defined. Figures 4.10 and 4.11 illustrate this development. By observation, the dislocation density in the cell walls increased as strain increased. This observation is in accordance with theoretical work which predicts that an increase in strain causes an increase in dislocation density [2,29,30].

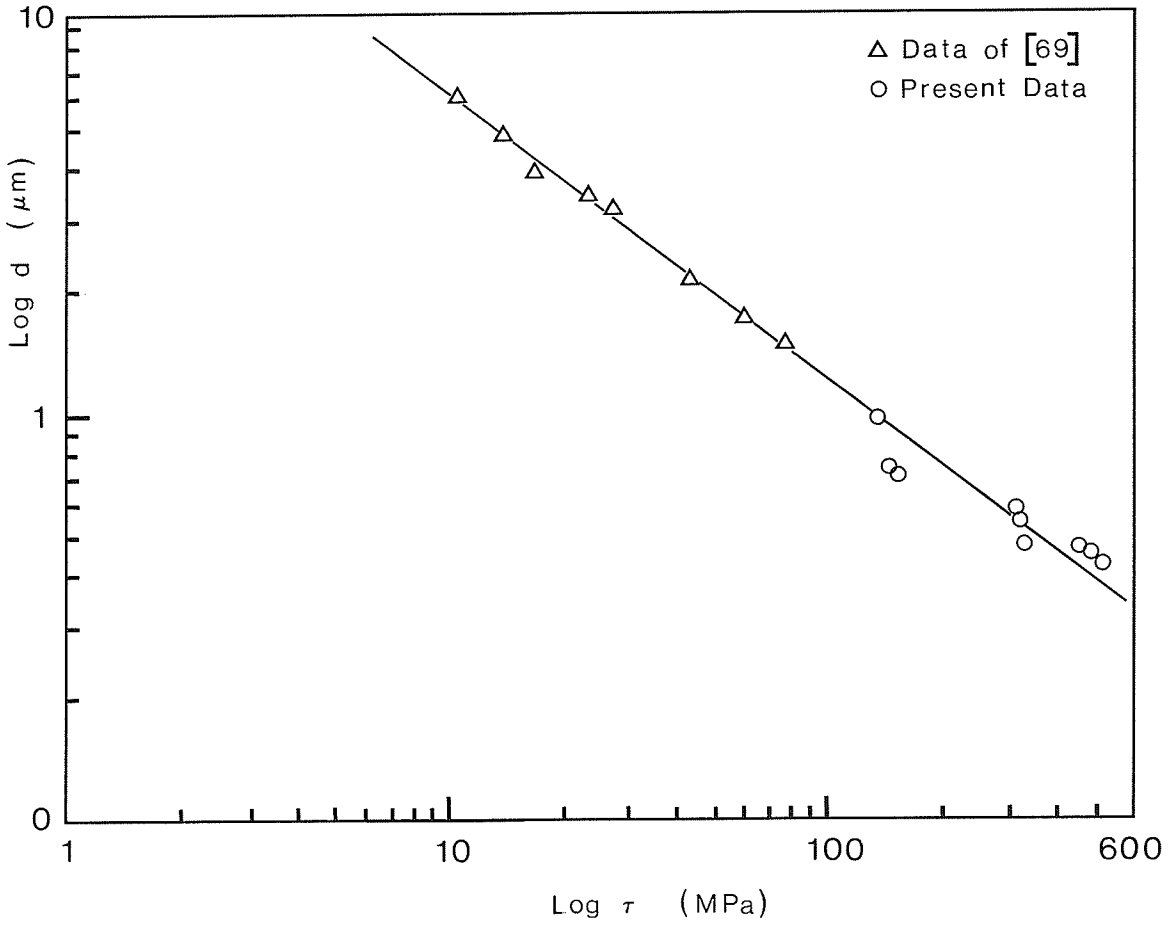

Figure 5.1: Relationship between Cell Size (L) and Shear Stress (τ)

Dislocation density and cell size are related by

$$L = k(\rho^{-1/2}) \qquad (11)$$

where L is dislocation cell size, ρ is dislocation density, and k is a constant [69]. Several studies have confirmed this relationship in copper [70,71,72,73].

Dislocation density is not homogeneous throughout a material during stage II of work hardening, and it has been reported that dislocation density in cell walls is between three and five times average density [69,74]. Knoesen and Kritzner have shown that as cell size decreases, so does the width of cell walls [74]. Their tensile tests on copper showed cell wall width was consistently 0.3 times the cell diameter during stage II. Cell wall definition improves as the width narrows. Straining increases the dislocation density and decreases cell size. Smaller cells have narrower, better defined walls.

5.1.3 Hierarchical Development of Dislocation Cell Walls

The dislocation cells continued to approximate the ideal low energy dislocation structure throughout stage II. This observation of similitude reinforces previous experimental work which identified similitude in steels [57,68]. Kuhlmann-Wilsdorf has described the process of forming smaller and smaller cells (similitude) with a hierarchical model [23]. In the present study, the theory of hierarchical development of dislocation walls was supported by three observations.

The foremost observation which supported the hierarchical dislocation structure was evidence of dislocation cell subdivision, as described by Kuhlmann-Wilsdorf [23]. Established dislocation cell walls were well defined with high dislocation density. Existing cells were seen to contain lesser developed dislocations walls, which created two neighbouring cells of similar diffraction contrast. An example of this occurrence is

shown in Figure 5.2, with arrows indicating the recently divided cells. Neighbouring cells of similar contrast indicate similar crystalline orientation, and suggests that sufficient cell rotation has not yet occurred. Cell rotation increases with cell wall development. Such evidence of cell subdivision in the present study strongly supports the theory of hierarchical formation of cell walls.

It was reported in previous work on various HSLA steels [57] that well developed dislocation cells occasionally pushed through a grain boundary. The ability of a dislocation cell to extend across a grain boundary at high strains was found to be evidence of general yielding in a ductile material. Such behaviour of dislocation cells was not observed in the present study. Relative microhardness measurements and TEM observations performed in this study showed the grain boundaries of commercial copper were sufficiently strong to restrain dislocation structures within grains. Relative microhardness measurements of grain boundaries and grain interiors, though approximate, support the statement that the grain boundaries were harder, and therefore stronger, than the grain interiors. TEM observations showed dislocation cells used grain boundaries as a cell wall. The grain boundaries were an integral part of the dislocation structure. Grains acted as the most primitive dislocation cell during hierarchical cell development. The function of grain boundaries to confine dislocation cell structures agrees with the premise of hierarchical dislocation structure development.

A final observation concerning grain boundaries and hierarchical dislocation cell development was the influence of grain size on the initial size of dislocation cells. The larger grain material initially produced larger dislocation cells for the same amount of strain, as compared to the smaller grain material. This trend was revealed for all three nominal strain rates used in the present study, as shown in Figure 4.14. By hierarchical development, the grain boundaries remained constant microstructural features and

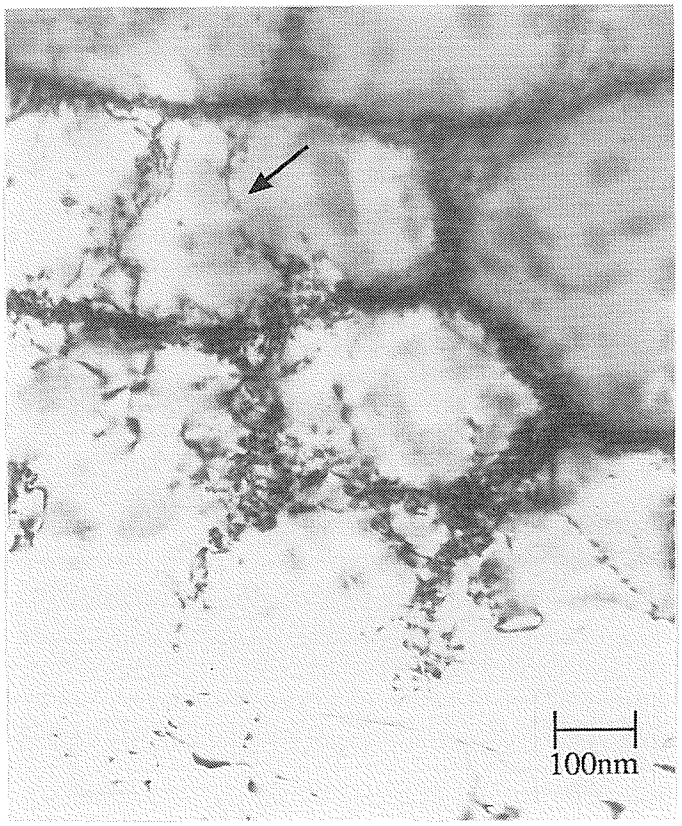

Figure 5.2: Hierarchical Cell Division

dislocation cells formed within each grain. The grain boundaries served as barriers to slip bands [75] and limited the dislocation movement. The restricted mobility caused by the grain boundaries was more acute in the smaller grain material and induced a smaller initial cell size. The difference in the dislocation cell size of the two grain size materials, at the same strain and crosshead speed, was pronounced during initial cell formation and diminished as the dislocation cell size approached minimum size. The correspondence of larger grain size with larger initial dislocation cell size supports the principle of hierarchical dislocation cell development.

The present study identified three pieces of supportive evidence for the understanding of cell formation by hierarchy as described by Kuhlmann-Wilsdorf, namely dislocation cell subdivision without noticeable cell rotation, the impermeability of grain boundaries to dislocation cell walls, and the influence of grain size on initial dislocation cell size. The observations suggested that the dislocation cells studied in commercial copper evolved by hierarchical subdivision.

5.1.4 Hall-Petch Type Relation for Substructure

The effect of the grain size on initial cell size, mentioned in the previous section, indicated that the larger grain material initially produced larger cells. The influence of grain size on material properties is often written in the form of the Hall-Petch equation, which is:

$$\sigma_y = \sigma_o + k(D^{-1/2}) \qquad (12)$$

where σ_y is yield stress, σ_o is frictional stress, k is a constant, and D is grain size. This relation is based on a model of yielding caused by dislocation pile-ups exerting sufficient force at grain boundaries to transfer plastic deformation from one grain to another.

A study by Li [76] obtained a Hall-Petch type of equation which related stress applied to dislocations (τ-τ_o), rather than yield stress, to grain size. The stress necessary to drive a dislocation pile-up through a tilt boundary was compared to the stress required to move dislocations through a Taylor-type forest, and it was found that a Hall-Petch relation could be applied to substructures. Li's relationship assumes dislocations are generated at grain boundaries and initial dislocation density is inversely proportional to grain size, as shown by experimental evidence. The following equation relates the stress applied to dislocations (τ-τ_o) to grain size (D):

$$\tau-\tau_o = \alpha G b(D^{-1/2}) \qquad (13)$$

where α is a constant, G is the shear modulus, and b is the Burgers vector [9].

Equation (6) described dislocation cell size to be inversely proportional to applied stress. A comparison of Equations (6) and (13) shows a relationship between dislocation cell size and grain size. At a given applied shear stress, dislocation cell size is proportional to the square root of grain size. Thus, the observation of larger dislocation cells in the larger grain material is consistent with these equations.

The larger grain material held larger dislocation cells, in the range of lower reduction in area values (smaller strain). However, the effect of grain size on dislocation cell size was not evident over the entire range of reduction in area values examined. The effect diminished as the dislocation cell size decreased. Ultimately, at reduction in area values greater than 40%, the dislocation cells were not differentiable by grain size of the material.

The dependence of flow stress on substructure size, rather than grain size, has been studied in nickel by Thompson [77]. It was found that flow stress followed the traditional Hall-Petch relation in material with grain size larger that 1.0 μm. In smaller grain material, flow stress was proportional to cell size. Dislocation cells were stronger than grains of the same size. Thompson explained this phenomenon by stating that flow stress is higher when dislocation source lengths are shorter, and that the dislocation source lengths are shorter in dislocation cells than in grain boundaries. Combining Equations (4), (5), and (6) of the meshlength theory reveals flow stress inversely proportional to dislocation source length during similitude.

$$\tau-\tau_O = \alpha Gb(l_S^{-1}) \tag{14}$$

By rewriting Equation (6) with a general exponent, m, for cell size, L, the following equation may be obtained [78]:

$$\tau-\tau_O = kGb(L^{-m}) \tag{15}$$

The exponent equals one when similitude is evident, as usual. However, the exponent takes a different value when similitude ceases.

In the present study, similitude ceased at a dislocation cell size of 0.4 μm, and shortly thereafter subgrains appeared. Dislocation cells transformed by polygonization into a subgrain structure. Subgrains had high angle boundaries and a degree of boundary perfection far superior to dislocation cells. The high angle boundaries of subgrains were akin to grain boundaries. Grain boundaries were associated with an exponent m of 1/2 as shown by the form of the original Hall-Petch equation. The occurrence of subgrains would suggest a shift in the exponent m from 1 to 1/2.

Subgrains were found in the copper specimens after the minimum cell size of 0.4 μm was attained. The work of Young and Sherby [79] indicated that for steels, subgrain boundary strengthening became the predominant load carrying mechanism at substructure sizes on the submicron range. Their comparison of the strength of grains and subgrains at various sizes revealed that at sizes smaller that 0.4 μm, subgrain boundaries became stronger than grain boundaries. Even though the results of Young and Sherby were for steels, they indicate the significant strengthening potential available once subgrain boundaries form.

The application of a Hall-Petch type equation for the study of substructure size and applied shear stress revealed two points. Firstly, when similitude was active and the exponent m equaled 1, the dislocation cell size was found to be proportional to the square root of the grain size. Secondly, upon the formation of subgrains the exponent m shifted from 1 to 1/2. The transition occurred when the dislocation cells were fully developed and additional plastic deformation produced subgrains. Subgrains became the bearer of the applied stress at these large stains, whereas the dislocation cells carried the load at lower strains.

5.1.5 Effect of Strain Rate Variation

The six specimen classifications of the present study were obtained by varying the grain size and the crosshead speed used during tensile testing. The effect of grain size variation, as described in the previous section, was found to be noteworthy, however no significant variation of nominal strain rate was observed in the present study.

It was anticipated in the present study that a decrease in strain rate would produce accelerated similitude. The present study did not illustrate the influence of strain rate variation of the dislocation cell size. The lack of visible evidence for the effect of strain

rate variation on dislocation cell size was due to the small range of only one decade in total variation in strain rate.

5.1.6 Minimum Dislocation Cell Size

Minimum dislocation cell size of the commercial copper was consistently found to be 0.4 μm. Dislocation cells of similar size (0.28 - 0.61 μm) have been measured in cyclically deformed copper [64]. The minimum cell size for copper was in the same order of magnitude as the minimum cell sizes of HSLA steels (0.4 μm) [57], AISI 4340 steels (0.4 - 0.5 μm) [68], and single crystal beryllium (1.0 μm) [56], pulled to failure in tension. The comparison indicated that it was reasonable to obtain a minimum dislocation cell size in the submicron range.

5.1.7 Indications of the End of Stage II

Dislocation cell measurements taken during the present study spanned a wide range of strains and emphasized the higher strain values near fracture. Dislocation cell sizes shrank in accordance with similitude at lower strains. The rate of change in dislocation cell size decreased as reduction in area (strain) increased, as shown in Figure 4.11. Similitude ceased to operate entirely as dislocation cells reached minimum size, at reduction in area values greater than 40%. For all six specimen classifications used in the present study, the minimum dislocation cell size was consistently found to be 0.4 μm. It was suggested by Kuhlmann-Wilsdorf [2] that similitude would eventually cease. The occurrence of a minimum cell size has been reported in several studies [57,68].

The dislocation cell size versus reduction in area curves (Figure 4.11) clearly illustrate similitude and the breakdown of similitude beyond 40% reduction in area. Other curves obtained in the present study also showed a knee in the range of 40%

reduction in area. Microhardness is indicative of internal stress or resistance to further deformation. It has been shown that a hardness curve plotted against true strain has a shape similar to a true strain curve [80]. Microhardness curves show monotonic increase with increasing reduction in area, and a decrease in slope at approximately 37% reduction in area, as shown in Figure 4.15. Beyond 37% reduction in area, the microhardness of the specimens continued to increase, but at a reduced rate.

Diameter profiles of the broken specimens also showed a change in material behaviour commencing at approximately 40% reduction in area. Diameter profiles, such as Figure 4.16, indicated that the specimens were deformed uniformly with the exception of the necked region. In all specimens, it was found that necking began when the specimen diameter reached 36 to 42% reduction in area. Necking marked the onset of tensile instability in the material. In the necked region, the stress was no longer uniaxial; triaxial stresses were active [37]. The transition from uniaxial stress to triaxial stress was made evident by the phenomena of necking, and occurred at approximately 40% reduction in area.

Deviations in material behaviour of commercial copper tensile specimens have been found in the 35 to 45% range of reduction in area. In this range, tensile instability became active causing a complex stress state in the necked region. Microhardness curves showed a decrease in slope in the same range of reduction in area. These examples of changes in material behaviour correspond with changes in material microstructure as defined by the dislocation cells. In the same range of reduction in area values, the phenomenon of similitude ceased to operate. Dislocation cells did not shrink appreciably beyond 40% reduction in area despite the continuous increase in true stress. At reduction in area values greater than 40%, the dislocation cells maintained a constant size of 0.4 μm.

5.1.8 Reasoning for the End of Stage II

Plausible causes for the breakdown of similitude include exceeding the upper bound of some property supporting the mechanical stability of the dislocation cell structure and the availability of a new low energy dislocation configuration more favourable than a cell structure [2]. The dislocation cells observed in the present study did not suffer decay or disintegration as similitude ceased. They remained intact and clearly visible well into the strain range where minimum cell size existed. Therefore, exceeding the mechanical stability of the dislocation cell structure was not observed to be the cause for the breakdown of similitude. Secondly, the availability of a LEDS with lower energy than a cell structure did not appear to cause the breakdown of similitude either. Subgrain structures are LEDS and were observed nestled with cell structures at high reduction in area values. However, subgrains occurred after minimum cell size was attained. Therefore, subgrains did not cause the end of similitude.

Similitude ceased when the dislocation cells stopped subdividing. The continued development of dislocation cells may have simply become inoperative. Glide dislocation interaction becomes less frequent as cell size decreases, since mobile dislocations are drawn into cell walls [2,32]. The tendency of free dislocations to be drawn into cell walls increases as cell interiors become smaller. Ultimately, at minimum cell size, no free dislocations are stable. The close proximity of cell walls induces dislocations to enter the wall structure. With no nucleation sites for new cell walls, the average dislocation cell size stabilizes. This reasoning for the occurrence of minimum cell size is in agreement with the meshlength theory, and has been adopted in the present study.

The lack of new nucleation sites for dislocation walls is taken to be the reason for the breakdown of similitude in this study. Individual dislocations were drawn into cell

walls, and cells were unable to subdivide further when the minimum cell size of 0.4 μm was achieved.

5.1.9 Subgrain Formation

Dislocation structure examination, in the range where the dislocation cell size remained constant, revealed a stable consistent cell structure with a subgrain structure occasionally interspersed amongst the dislocation cells. The physical characteristics which set subgrains apart from dislocation cells were their overall shape and the condition of the dislocation boundaries. The appearance of subgrains indicated significant rearrangement of dislocations in the metal. Dislocation cells were circular and especially uniform at high values of reduction in area. Cell walls were made up of many individual dislocations. The cell walls and interior were clearly distinguishable. In contrast, the subgrains were not circular. Subgrains were present in shapes similar to a football with acute corners. The subgrain boundaries were thin, crisp, and clear during TEM observation. The clarity of the two types of structures ensured accurate identification.

Subgrains were observed only at the highest values of reduction in area. Subgrains have been identified as low energy configurations formed in highly deformed material and have been associated with a recently defined stage IV of work hardening [12]. The strain value at which subgrain formation commences has been found to vary with the type of metal [9]. Subgrains, formed by the process of polygonization, evolve from dislocation cells [9]. Higher stresses cause cell rotations, and the crystalline misorientation between adjacent cells increases. Low angle boundaries reach a critical angle, and consequently the transition from dislocation cell wall to subgrain boundary is made. Subgrain formation is indicative of large strain.

The existence of minimum-sized dislocation cells and the formation of subgrains occurred in the necked region of the tensile specimens. The actual stress values in the necked region were not known. The stress at the onset of minimum dislocation cell size is represented by Equation (6). The stress at the maximum dislocation density is represented by the form of Equation (2). Since the minimum dislocation cell size and the formation of subgrains were observed simultaneously in TEM foils, it was surmised that the critical stresses for both structures were at least close in magnitude.

The present study observed subgrain formation following the achievement of minimum dislocation cell size in commercial copper. Subgrain formation from dislocation cells is possible by polygonization. The critical stress for subgrain formation and for minimum cell size are expected to be of similar magnitude, since the two substructures occur simultaneously and in near proximity of each other.

5.2 Mechanisms of Fracture

It was thought that the crack path may have followed the dislocation cell walls, but it was found that fracture was initiated at inclusion sites and progressed as typical ductile fracture.

5.2.1 Involvement of Dislocation Cells During Fracture

The copper tensile specimens were subjected to severe plastic deformation in the necked region prior to fracture. Fracture occurred in the necked region where well defined dislocation structures also formed. The contribution of dislocation cells to the fracture process was investigated, as follows.

A comparison of dimple size on the fracture surface and dislocation cell size at fracture determined if the crack path followed the walls of the dislocation cell structure. It was expected that if the crack path was dependent on the dislocation cell structure, then the size of the fracture surface dimples and the size of the dislocation cells would be of the same order of magnitude. The fracture surface dimples were measured and found to be in the order of 6 μm (equivalent diameter). Dislocation cells were known to be 0.4 μm at fracture, since they had attained their minimum size at 40% reduction in area. The two parameters were not close in magnitude. Thus, it was deduced that the final fracture process was not related to the dislocation cells, and the development of dislocation structures was truncated when the tensile specimens fractured.

5.2.2 Void Initiation at Inclusions

The copper tensile specimens in the present study failed by ductile fracture. Extensive plastic deformation accompanied the fracturing of the tensile specimens, and all specimens fractured in the highly deformed necked region. The microscopic texture of the fracture surface was dimpled. The dimple size was too large to be caused by dislocation cells. However, dimples frequently contained an inclusion, and dimple size was observed to be proportional to the size of the resident inclusion. The fracture surface provided the information required to determine the fracture process of the copper tensile specimens.

The dimpled fracture surfaces were characteristic of ductile fracture in a ductile material with brittle inclusions. The dimples often contained a single resident inclusion. Some of the inclusions, particularly the larger ones, were broken in a brittle manner. The dimples were polygonal in shape and often elongated. The dimples were contiguous, and boundaries between dimples were formed by a tapered ridge of ruptured matrix. Each of

these characteristics gave insights to the state of the material and the mechanisms active during fracture.

The inclusions were identified as the weak link in the chain of material strengths. The fracture surfaces of the present study were similar to those studied by Puttick [41] who also tested commercial tough pitch copper in tension. Fractured and whole inclusions were found in the dimples in both studies. Voids were initiated by either fracture of the inclusion or by inclusion-matrix decohesion. Brittle inclusions imbedded in a ductile matrix have been found to break with a small amount of plastic deformation [9]. Indeed, an example of fractured inclusions found in the present study is shown in Figure 4.8. Void initiation also occurred at the inclusion-matrix interface. An example of interfacial separation was captured in a TEM photograph. Figure 4.13 shows a pile-up of dislocations against the inclusion and depicts the inception of a void. Voids were initiated at inclusions, and these voids were ultimately responsible for the fracturing of the copper tensile specimens.

Inclusion size may have been the deciding factor in determining which of the two mechanisms of void initiation at inclusions was triggered. In the present study, the average inclusion was in the order of 1 μm. Large inclusions fractured and caused void initiation at the stress concentrations imposed in the matrix. The smaller inclusions were found to be whole, suggesting void initiation by decohesion of the inclusion-matrix interface. The results of the present study were consistent with those of Goods and Brown who reported that particles larger than 1 μm fracture and particles smaller than 1 μm are prone to interfacial decohesion [44].

In the present study, final fracture was caused by the coalescence of voids which were initiated at inclusions. The voids were initially created by either inclusion breakage or inclusion-matrix decohesion. The mechanism for void initiation was related to the

inclusion size. The voids enlarged, and the copper ligaments separating the voids eventually ruptured, creating the dimpled fracture surfaces.

5.2.3 Dimple Shape

The shape of dimples on a fracture surface indicate if voids coalesced as ligaments of material between them ruptured or if voids linked together as material sheared [81]. Dimples of both types were found on the copper fracture surfaces (Figure 4.7). The macroscopic 45° planar surfaces held shear rupture dimples. Dimples resulting from normal rupture were found at the intersections of shear planes, at the peaks and valleys towards the center of the specimen.

Dimples on the inclined planes of the fracture surface were formed by linkage of voids during localized shear. In shape, these dimples had one side at a significantly different elevation than the other. They cascaded down the shear plane towards the outside radius of the tensile specimen. The distorted shape of these dimples indicated the gross plastic deformation suffered during the fracture process. Localized shear combined with inclusions resulted in confined localized shear bands where void growth was facilitated. Voids coalesced in the most active shear bands, producing the inclined fracture surfaces.

Dimples formed by normal rupture were enclosed by tapered walls of material of the same approximate height and were nonuniform in shape. The copper ligaments between voids necked down on the microscopic scale [9,40]. The process of necking between voids was akin to the formation of a knife edge by uninhibited slip in a pure metal [82]. The voids enlarged as the microscopic internal necking continued. The fracture surface formed when the voids became contiguous and the copper ligaments

ruptured. The random shape of these dimples reflected the nonuniform triaxial stress state during fracture [9].

5.3 Summary of Deformation and Fracture Processes

In the present study, tensile specimens of commercial purity copper were pulled to failure. Dislocation cell behaviour during plastic deformation was characterized using TEM investigation. Mechanisms responsible for final fracture were identified using SEM examination.

Increase in plastic deformation in the tensile specimens, induced the formation of low energy dislocation structures. Dislocation cells formed at all reduction in area values examined, without exception. Evolution of the dislocation cell structure was studied with reference to variation in reduction in area (strain). It was found that the dislocation cell structure obeyed similitude, until a minimum cell size was attained at approximately 40% reduction in area. The minimum cell size was consistently found to be 0.4 μm for the specimens tested in this study.

Reduction in cell size was achieved by hierarchical development within the dislocation structure. Dislocation cells were subdivided by formation of new cell walls within existing cells. Larger grain material produced initially larger dislocation cells, and all dislocations structures reached the same minimum cell size. The effect of grain size on initial cell size supports the principle of hierarchical cell development.

Similitude was accompanied by improved resolution of cell walls. Dislocation density within the walls increased with strain. Fully developed dislocation cell structures consisted of networks of dense dislocations. Beyond 45% reduction in area, minimum cell size was achieved and sporadic subgrain formation was observed. Minimum

dislocation cell size indicated that stage II ended and stage III had been reached. Subgrains were immediately distinguishable from dislocation cells by their distinctive shape.

Dislocation structure development was halted abruptly when fracture was triggered. It was determined that the fracture mechanisms were not related to the dislocation structures. Using SEM, the fracture surface dimple size was measured. The fracture surface dimple size was in the order of ten times larger than the dislocation cell size at fracture. The gross difference in size eliminated the possibility of dislocation structures playing a significant role in the fracture process.

The fracture of the copper tensile specimens was typical of ductile fracture. Inclusions, inherent to commercial copper, proved to be the particles responsible for initiating fracture. Inclusions in the necked region were the sites for void initiation. Particle size determined if void initiation occurred at a fractured particle or at the particle-matrix interface. The triaxial and biaxial stress conditions in the necked region caused the voids to coalesce by either normal or shear rupture. The ligaments of copper between the voids deformed by microscopic necking or by shear, depending on the local stress state. The fracture surface was produced when the copper ligaments between the voids ruptured. The resulting fracture surface was covered with dimples which frequently held the inclusion that induced their formation.

6. CONCLUSIONS

The fundamental objective of the present study was to characterize the development of dislocation cells formed in commercial copper during plastic deformation. Commercial copper tensile specimens with two grain sizes were tested at three crosshead speeds to produce six specimen classifications. The Klassen specimen sectioning technique was used in order to obtain a range of reduction in area values from each specimen. The study revealed significant information regarding the evolution of dislocation cells during plastic deformation, including characteristic curves of dislocation cell size versus reduction in area. The study also revealed the basic mechanisms involved in the final fracture.

The results of the present study were in good agreement with previous studies of low energy dislocation structures. In light of the theory of work hardening developed by Kuhlmann-Wilsdorf, the present study reinforced the principle of similitude, presented supportive evidence for the hierarchical development of dislocation cells, and documented the breakdown of similitude. Dislocation cells were observed to form and decrease in size, as strain (reduction in area) increased. The cells were approximately equiaxed. Strain induced further cell development. Cell wall definition improved; the walls became thinner and crisper. Dislocation cells were seen to subdivide into smaller cells. Rotation of adjacent cells was evident. The number of dislocation cell patches increased. Eventually, a minimum dislocation cell size emerged.

In addition to reinforcing current theories of low energy dislocation structures, the present study determined parameters particular to dislocation cell development in commercial copper subjected to tensile testing. It was found that for two grain sizes and three nominal strain rates, the dislocation cells in all specimens reached a minimum dislocation cell size of 0.4 μm. Minimum cell size was attained by 40% reduction in

area. Characteristic curves depicting development of dislocation cell size were obtained for the six specimen classifications.

Of the two experimental variables, grain size and nominal strain rate, one yielded positive results. The effect of grain size variation was found in the initial dislocation cell size at reduction in area values less than 40%, especially at the lower values. At the same reduction in area value, smaller dislocation cells formed in the finer grain material. The more closely spaced grain boundaries restricted dislocation mobility. The effect of strain rate variation was not found, due to an insufficient range of strain rates.

The fortuitous detection of subgrains was found at the highest reduction in area values. Beyond 45% reduction in area, after minimum dislocation cell size had been firmly established, occasional subgrain formation occurred. Subgrain formation by polygonization from dislocation cells was highly probable. The simultaneous existence of minimum sized dislocation cells and subgrain formation indicated qualitatively that the stress associated with the minimum cell size and the stress associated with maximum dislocation density were close in magnitude.

The present study also investigated the cause of fracture by examining the fracture surfaces of the copper tensile specimens. The fracture surface dimples were in the order of one magnitude larger than the dislocation cell size at fracture. Due to the gross difference in size, the likelihood of dislocation cells contributing to the final fracture process was eliminated. Examination of the fracture surfaces revealed that the inclusions served as sites for void initiation. The coalescence of these voids occurred at fracture and created the dimpled fracture surface. The process was typical of ductile fracture of a material with a ductile matrix and hard inclusions.

The present study examined the behaviour of commercial copper during plastic deformation, and characterized the development of dislocation structures in terms of the meshlength theory of Kuhlmann-Wilsdorf. The progressive development of the dislocation structures ceased when ductile fracture occurred, caused by void initiation at inclusions. The plastic deformation and fracture processes involved in the failure of commercial copper tensile specimens were investigated and determined in the present study.

REFERENCES

[1] E.C. Aifantis, in E.C. Aifantis and J.P. Hirth (eds.), *International Symposium on Mechanics of Dislocations, 28-31 August 1983*, American Society for Metals, 1985, p. 127.

[2] D. Kuhlmann-Wilsdorf, in J.P. Hirth and J. Weertman (eds.), *Work Hardening*, Gordon and Breach, New York, 1968, p. 97.

[3] J.D. Embury and F. Zok, in W.R. Tyson and B. Mukherjee (eds.), *Proceedings of the International Symposium on Fracture Mechanics, 23-26 August 1987*, Pergamon Press, Toronto, 1988, p. 1.

[4] R.N. Gardner, T.C. Pollock, and H.G.F. Wilsdorf, *Materials Science and Engineering*, 29(1977)169.

[5] D. Hull and D.J. Bacon, *Introduction to Dislocations*, Third Edition, Pergamon Press, Toronto, 1984.

[6] G.I. Taylor, *Proceedings of the Royal Society (London)*, A145(1934)362.

[7] N.F. Mott, *Philosophical Magazine*, 43(1952)1151.

[8] J.T. Fourie, P.J. Jackson, D. Kuhlmann-Wilsdorf, D.A. Rigney, J.H. van der Merwe, and H.G.F. Wilsdorf, *Scripta Metallurgica*, 16(1982)157.

[9] M.A. Meyers and K.K. Chawla, *Mechanical Metallurgy Principles and Applications*, Prentice-Hall Inc., Englewood Cliffs, New Jersey, 1984.

[10] S.K. Mitra and J.E. Dorn, *Transactions of the Metallurgical Society of AIME*, 224(1962)1062.

[11] J. Friedel and G. Saada, in J.P. Hirth and J. Weertman (eds.), *Work Hardening*, Gordon and Breach, New York, 1968, p. 1.

[12] J.G. Sevillano and E. Aernoudt, *Materials Science and Engineering*, 86(1987)35.

[13] F.R.N. Nabarro, in E.C. Aifantis and J.P. Hirth (eds.), *International Symposium on Mechanics of Dislocations, 28-31 August 1983*, American Society for Metals, 1985, p. 1.

[14] J.H. Weiner, in E.C. Aifantis and J.P. Hirth (eds.), *International Symposium on Mechanics of Dislocations, 28-31 August 1983*, American Society for Metals, 1985, p. 5.

[15] A. Seeger, in *The Relation Between the Structure and Mechanical Properties of Metals, 7-9 January 1963*, Her Majesty's Stationery Office, London, 1963, p. 4.

[16] A. Seeger, in J.P. Hirth and J. Weertman (eds.), *Work Hardening*, Gordon and Breach, New York, 1968, p. 27.

[17] Z.S. Basinski and S.J. Basinski, *Philosophical Magazine*, 9(1964)51.

[18] P.B. Hirsch and T.E. Mitchell, in J.P. Hirth and J. Weertman (eds.), *Work Hardening*, Gordon and Breach, New York, 1968, p. 65.

[19] C. Laird, in A.W. Thompson (ed.), *Work Hardening in Tension and Fatigue, 11 November 1975*, Metallurgical Society of AIME, New York, 1977, p. 150.

[20] J.I. Dickson, L. Handfield and G. L'Esperance, *Materials Science and Engineering*, 81(1986)477.

[21] P. Lukas, L. Kunz, and Z. Knesl, *Materials Science and Engineering*, 70(1985)91.

[22] D.A. Rigney, M.G.S. Naylor, R. Divakar, and L.K. Ives, *Materials Science and Engineering*, 81(1986)409.

[23] N. Hansen and D. Kuhlmann-Wilsdorf, *Materials Science and Engineering*, 81(1986)141.

[24] D. Kuhlmann-Wilsdorf, *Transactions of the Metallurgical Society of AIME*, 224(1962)1047.

[25] D. Kuhlmann-Wilsdorf, *Metallurgical Transactions*, 1(1970)3173.

[26] D. Kuhlmann-Wilsdorf and N.R. Comins, *Materials Science and Engineering*, 60(1983)7.

[27] D. Kuhlmann-Wilsdorf, J.H. van der Merwe, and H. Wilsdorf, *Philosophical Magazine*, 43(1952)632.

[28] M.N. Bassim, *Ph.D. Dissertation*, University of Virginia, 1973.

[29] D. Kuhlmann-Wilsdorf, in A.W. Thompson (ed.), *Work Hardening in Tension and Fatigue, 11 November 1975*, Metallurgical Society of AIME, New York, 1977, p. 1.

[30] D. Kuhlmann-Wilsdorf and J.H. van der Merwe, *Materials Science and Engineering*, 55(1982)79.

[31] D. Kuhlmann-Wilsdorf, *Metallurgical Transactions A*, 16A(1985)2091.

[32] H.G.F. Wilsdorf, *Materials Science and Engineering*, 59(1983)1.

[33] R.N. Gardner and H.G.F. Wilsdorf, *Metallurgical Transactions A*, 11A(1980)659.

[34] P.J. Jackson, *Materials Science and Engineering*, 81(1986)169.

[35] T. Hasegawa and U.F. Kocks, *Acta Metallurgica*, 27(1979)1705.

[36] R.W.K. Honeycombe, *The Plastic Deformation of Metals*, Edward Arnold, London, 1968.

[37] G.E. Dieter, *Mechanical Metallurgy*, Second Edition, McGraw-Hill Book Company, Toronto, 1976.

[38] W.H. Chen, *International Journal of Solid Structures*, 7(1971)685.

[39] D.M. Tracey, *Engineering Fracture Mechanics*, 3(1979)301.

[40] C.D. Beachem, in H. Liebowitz (ed.), *Fracture: An Advanced Treatise*, Academic Press, New York, 1968, p. 243.

[41] K.E. Puttick, *Philosophical Magazine*, 4(1959)964.

[42] L.M. Brown and J.D. Embury, *Proceedings of the Third International Conference on the Strength of Metals and Alloys, Cambridge, Cambs., 20-25 August 1973*, Iron and Steel Institute, Institute of Metals, London, 1974, p. 164.

[43] A.S. Argon, J. Im, and R. Safoglu, *Metallurgical Transactions A*, 6A(1975)825.

[44] S.H. Goods and L.M. Brown, *Acta Metallurgica*, 27(1979)1.

[45] J.R. Fischer and J. Gurland, *Metal Science*, 15(1981)185.

[46] J.R. Fischer and J. Gurland, *Metal Science*, 15(1981)193.

[47] D. Broek, *Engineering Fracture Mechanics*, 5(1973)55.

[48] T.C. Lindley, G. Oates, and C.E. Richards, *Acta Metallurgica*, 18(1970)1127.

[49] M.R. Piggott, *Load Bearing Fibre Composites*, Pergamon Press, Toronto, 1980.

[50] W.J. McGregor Tegart, *Elements of Mechanical Metallurgy*, The Macmillan Company, New York, 1967.

[51] J.I. Bluhm and R.J. Morrissey, *Proceedings of the First International Conference on Fracture, Sendai, 1965*, Volume III, Japan Society for the Strength and Fracture of Materials, Sendai, 1966, p. 1739.

[52] R.L. Lyles, Jr. and H.G.F. Wilsdorf, *Acta Metallurgica*, 23(1975)269.

[53] I.Y. Chan and H.G.F. Wilsdorf, *Acta Metallurgica*, 29(1981)1221.

[54] I.Y.T. Chan and H.G.F. Wilsdorf, *Materials Science and Engineering*, 49(1981)229.

[55] R.W. Bauer and H.G.F. Wilsdorf, *Scripta Metallurgica*, 7(1973)1213.

[56] T.C. Pollock and H.G.F. Wilsdorf, *Materials Science and Engineering*, 61(1983)7.

[57] R.J. Klassen, *M.Sc. Thesis*, University of Manitoba, 1985.

[58] M.N. Bassim, *Materials Science and Engineering*, 95(1987)199.

[59] American Society for Testing and Materials, *ASTM Standards*, Designation E8-85a, 1985.

[60] G.L. Kehl, *The Principles of Metallographic Laboratory Practice*, Third Edition, McGraw-Hill Book Company, Inc., Toronto, 1949.

[61] M.N. Bassim and R.J. Klassen, *Materials Science and Engineering*, 81(1986)163.

[62] M.N. Bassim, R.J. Klassen, M.R. Bayoumi, and H.G.F. Wilsdorf, *Materials Science and Engineering*, 92(1987)107.

[63] P.J. Goodhew, in A.M. Glauret, *Practical Methods in Electron Microscopy*, Volume II, Elsevier, New York, 1985.

[64] C.E. Feltner and C. Laird, *Acta Metallurgica*, 15(1967)1633.

[65] V.M. Faires, *Design of Machine Elements*, Fourth Edition, Macmillan Company, New York, 1965.

[66] Metals Handbook, *Properties and Selection: Nonferrous Alloys and Pure Metals*, Ninth Edition, Volume 2, American Society for Metals, Metals Park, Ohio, 1979.

[67] M.N. Bassim and R.J. Klassen, *Scripta Metallurgica*, 21(1987)625.

[68] M.N. Bassim and X.B. Huang, *Materials Science and Engineering*, 96(1987)159.

[69] M.R. Staker and D.L. Holt, *Acta Metallurgica*, 20(1972)569.

[70] W.M. Stobbs, J.S. Kallend, and J.A. Williams, *Acta Metallurgica*, 24(1976)1083.

[71] D.A. Rigney, *Scripta Metallurgica*, 13(1979)353.

[72] A. van den Beukel, *Scripta Metallurgica*, 13(1979)83.

[73] T. Ungar, L.S. Toth, J. Illy, and I. Kovacs, *Acta Metallurgica*, 34(1986)1257.

[74] D. Knoesen and S. Kritzinger, *Acta Metallurgica*, 30(1982)1219.

[75] R.W. Armstrong, *Canadian Metallurgical Quarterly*, Volume 13, Number 1(1974)187.

[76] J.C.M. Li, *Transactions of the Metallurgical Society of AIME*, 227(1963)239.

[77] A.A.W. Thompson, *Acta Metallurgica*, 23(1975)1337.

[78] A.W. Thompson, *Metallurgica Transactions A*, 8A(1977)833.

[79] C.M. Young and O.D. Sherby, *Journal of Iron and Steel Institute*, September(1973)640.

[80] D. Tabor, *Journal of the Institute of Metals*, 79(1951)1.

[81] C.D. Beacham, *Metallurgical Transactions A*, 6A(1975)377.

[82] H.G.F. Wilsdorf, *Acta Metallurgica*, 30(1982)1247.